

# Tri-Hybrid Multi-User Precoding Using Pattern-Reconfigurable Antennas: Fundamental Models and Practical Algorithms

Pinjun Zheng, Yuchen Zhang, Tareq Y. Al-Naffouri, Md. Jahangir Hossain, and Anas Chaaban

**Abstract**—The integration of pattern-reconfigurable antennas into hybrid multiple-input multiple-output (MIMO) architectures presents a promising path toward high-efficiency and low-cost transceiver solutions. Pattern-reconfigurable antennas can dynamically steer per-antenna radiation patterns, enabling more efficient power utilization and interference suppression. In this work, we study a tri-hybrid MIMO architecture for multi-user communication that integrates digital, analog, and antenna-domain precoding using pattern-reconfigurable antennas. For characterizing the reconfigurability of antenna radiation patterns, we develop two models—Model I and Model II. Model I captures realistic hardware constraints through limited pattern selection, while Model II explores the performance upper bound by assuming arbitrary pattern generation. Based on these models, we develop two corresponding tri-hybrid precoding algorithms grounded in the weighted minimum mean square error (WMMSE) framework, which alternately optimize the digital, analog, and antenna precoders under practical per-antenna power constraints. Realistic simulations conducted in ray-tracing generated environments are utilized to evaluate the proposed system and algorithms. The results demonstrate the significant potential of the considered tri-hybrid architecture in enhancing communication performance and hardware efficiency. However, they also reveal that the existing hardware is not yet capable of fully realizing these performance gains, underscoring the need for joint progress in antenna design and communication theory development.

**Index Terms**—pattern-reconfigurable antennas, tri-hybrid MIMO, multi-user precoding, per-antenna power constraint.

## I. INTRODUCTION

Since their inception in the 1990s, multiple-input multiple-output (MIMO) technologies have become a cornerstone of modern wireless communication systems [1]. By deploying multiple antennas at both the transmitter and receiver, MIMO systems leverage spatial diversity to mitigate fading and enhance link reliability, while employing spatial multiplexing to transmit independent data streams in parallel, thereby significantly improving spectral efficiency under constraints on bandwidth and power. These advantages have led to the widespread adoption of MIMO in wireless standards such as LTE, 5G NR, and Wi-Fi [2]–[4]. As communication systems

shift toward higher-frequency bands, such as mmWave, large-scale antenna arrays are necessary to overcome increased path loss, which introduces challenges in hardware cost and system complexity. To address this problem, hybrid beamforming architecture has emerged as a promising solution, combining digital and analog processing to approximate the performance of fully digital systems while using a reduced number of radio frequency (RF) chains [5]–[7]. With the ongoing evolution toward massive MIMO [8], extra-large-scale massive MIMO [9], and the growing emphasis on energy and cost efficiency in the future sixth generation (6G) [10], the development of more efficient transceiver architectures remain a key research focus.

Over the years, numerous innovative antenna designs have been explored for integration into MIMO transceiver architectures, including pattern-reconfigurable antennas [11], reconfigurable holographic surfaces [12], dynamic metasurface antennas [13], and fluid antennas [14], among others. These efforts aim to introduce additional degrees of freedom at the antenna layer by leveraging reconfigurable antennas to achieve more desirable radiation characteristics. In fact, reconfigurable antennas have long been studied within the antenna community [15], [16], but their integration into modern MIMO systems has only recently begun to receive significant attention. For example, the authors of [17] investigate the application of pattern-reconfigurable antennas in massive MIMO systems, demonstrating substantial throughput gains for multi-user transmission with low channel estimation overhead. A polarization reconfigurable antenna system is studied in [18], where polarization reconfigurability is shown to effectively mitigate mismatch, leading to considerable enhancements in overall communication performance. Given the additional flexibility introduced by reconfigurable antennas, their integration into hybrid MIMO architectures gives rise to a novel *tri-hybrid architecture* [19], which holds strong potential as a high-efficiency solution for emerging 6G applications. A few early explorations have already been reported. For instance, a tri-hybrid precoding architecture based on dynamic metasurface antennas was investigated in [20], where joint design of digital, analog, and antenna-domain precoders was shown to reduce the number of RF chains and phase shifters while improving energy efficiency.

Among the reconfigurable antennas discussed above, *pattern-reconfigurable antennas* stand out as particularly promising candidates for tri-hybrid integration. By dynamically steering energy toward intended directions, these antennas enable more efficient power utilization and more ef-

Pinjun Zheng, Md. Jahangir Hossain, and Anas Chaaban are with the School of Engineering, The University of British Columbia, Kelowna, BC V1V 1V7, Canada (e-mail: pinjun.zheng@ubc.ca; jahangir.hossain@ubc.ca; anas.chaaban@ubc.ca). Yuchen Zhang and Tareq Y. Al-Naffouri are with the Electrical and Computer Engineering Program, Division of Computer, Electrical and Mathematical Sciences and Engineering (CEMSE), King Abdullah University of Science and Technology (KAUST), Thuwal, 23955-6900, Kingdom of Saudi Arabia (e-mail: yuchen.zhang@kaust.edu.sa; tareq.alnaffouri@kaust.edu.sa).

fective interference suppression than their fixed-pattern counterparts [21]. Recent advances in the prototyping and experimental validation of pattern-reconfigurable antennas have further demonstrated these advantages [22]. Nevertheless, tri-hybrid precoding solutions that leverage pattern-reconfigurable antennas remain insufficiently explored. A theoretical investigation into pattern-reconfigurable antenna-based tri-hybrid beamforming was presented in [23]. While the results are promising, the approach in [23] relies on discretizing radiation patterns in the angular domain, which leads to a prohibitively large-size effective channel matrix, particularly in three-dimensional (3D) real space, resulting in significant computational challenges. Moreover, the study assumes a half-wavelength-spaced antenna array composed of elements whose physical sizes exceed half a wavelength, potentially yielding overly optimistic performance estimates. Therefore, more tractable modeling, efficient precoding algorithms, and realistic evaluations remain essential for advancing this technology toward practical deployment. To address these gaps, this paper investigates the tri-hybrid multi-user precoding problem with pattern-reconfigurable antennas, presenting a comprehensive study that encompasses fundamental modeling, practical algorithm design, and realistic performance evaluation.

The main contributions of this paper are as follows:

- To establish a comprehensive foundation, we develop two models to characterize per-antenna radiation pattern reconfigurability within the tri-hybrid MIMO architecture. The first model captures limited pattern selection, reflecting the operational principles of practical reconfigurable antennas and enabling realistic performance evaluation. The second model permits arbitrary radiation pattern generation via spherical harmonics decomposition, representing an idealized upper bound that may become achievable with future hardware advancements. Both models provide more tractable formulations compared to existing approaches, without introducing significant additional complexity. Furthermore, the derivation clearly shows how our models naturally reduce to the conventional MIMO channel model, ensuring backward compatibility with prior work on traditional hybrid MIMO systems.
- Using our developed models, we design two precoding algorithms based on the weighted minimum mean-square error (WMMSE) framework. These algorithms jointly optimize the digital, analog, and antenna-domain precoders in an alternating fashion, and incorporate practical *per-antenna power constraints*, in contrast to the *sum-power constraint* commonly assumed in the literature. Both algorithms exhibit quadratic (rather than exponential) complexity with respect to the number of base station (BS) antennas, ensuring their practicality in large-scale MIMO systems.
- We conduct extensive simulations to validate the considered tri-hybrid MIMO system and the proposed algorithms. A ray-tracing-based channel generation is employed to emulate realistic propagation environments. Our simulations aim to answer the following key questions:

**Q1** How much performance gain can be achieved by

incorporating pattern-reconfigurable antennas into multi-user hybrid MIMO systems, under both (i) current practical hardware limitations and (ii) ideal scenarios without any hardware limitation?

**Q2** Can the introduction of reconfigurable radiation patterns reduce the required number of costly RF chains and antennas without compromising performance?

The remainder of this paper is organized as follows. Section II introduces the general signal and channel models. Section III extends the channel model to incorporate antenna radiation pattern reconfigurability, leading to the proposed Model I and Model II. Based on these two models, we propose corresponding tri-hybrid precoding algorithms in Sections IV and V, respectively. Simulation results are presented in Section VI, and conclusion is drawn in Section VII.

We adopt the following notation throughout the paper. Nonbold italic lower and upper case letters (e.g.,  $a$ ,  $A$ ) denote scalars, bold lower case letters (e.g.,  $\mathbf{a}$ ) denote vectors, and bold upper case letters (e.g.,  $\mathbf{A}$ ) denote matrices. We use  $[\mathbf{A}]_{i,j}$  to denote the entry at the  $i^{\text{th}}$  row and  $j^{\text{th}}$  column of the matrix  $\mathbf{A}$ . In addition,  $[\mathbf{A}]_{n,:}$  and  $[\mathbf{A}]_{:,m}$  denote  $n^{\text{th}}$  row and  $m^{\text{th}}$  column of  $\mathbf{A}$ , respectively. The superscripts  $(\cdot)^{\text{T}}$ ,  $(\cdot)^*$ ,  $(\cdot)^{\text{H}}$ , and  $(\cdot)^{-1}$  represent the transpose, conjugate, Hermitian (conjugate transpose), and inverse operators, respectively. The notations  $\|\cdot\|_0$ ,  $\|\cdot\|_2$ , and  $\|\cdot\|_{\text{F}}$  denote the  $\ell_0$  quasi-norm, the  $\ell_2$  norm, and the Frobenius norm, respectively. Additionally,  $\text{Tr}(\cdot)$  denotes the trace of a square matrix,  $\text{Re}(\cdot)$  returns the real part,  $\odot$  denotes the Hadamard (element-wise) product, and  $\otimes$  represents the Kronecker product.

## II. SIGNAL AND CHANNEL MODELS

As illustrated in Fig. 1, we consider a downlink multi-user MIMO system where an  $N$ -antenna BS simultaneously serves  $K$  user equipments (UEs), each equipped with  $M_k$  antennas. Unlike conventional digital-analog hybrid precoding, this work further incorporates antenna radiation pattern reconfigurability at the BS, allowing each antenna's radiation pattern to be independently controlled. Before analyzing the impact of radiation pattern reconfigurability, this section first outlines the adopted signal and channel models.

### A. Signal Model

Consider a BS equipped with  $N_{\text{RF}}$  RF chains and  $N$  RF phase shifters. Assume that the  $k^{\text{th}}$  UE requires  $D_k$  data streams, and let  $\mathbf{s}_k \in \mathbb{C}^{D_k}$  denote this data stream vector. We concatenate all of these data vectors and define  $\mathbf{s} = [\mathbf{s}_1^{\text{T}}, \mathbf{s}_2^{\text{T}}, \dots, \mathbf{s}_K^{\text{T}}]^{\text{T}} \in \mathbb{C}^D$ , where  $D = \sum_{k=1}^K D_k$  and we assume  $\mathbb{E}[\mathbf{s}\mathbf{s}^{\text{H}}] = \mathbf{I}_D$ . Let  $\mathbf{F}_{\text{BB}} \in \mathbb{C}^{N_{\text{RF}} \times D}$  denote the baseband digital precoder and  $\mathbf{F}_{\text{RF}} \in \mathbb{C}^{N \times N_{\text{RF}}}$  denote the RF analog precoder. Then, the signals fed into the  $N$  transmit antennas can be written as [6], [24]

$$\mathbf{x} = \mathbf{F}_{\text{RF}}\mathbf{F}_{\text{BB}}\mathbf{s} = \sum_{k=1}^K \mathbf{F}_{\text{RF}}\mathbf{F}_{\text{BB},k}\mathbf{s}_k, \quad (1)$$

where  $\mathbf{F}_{\text{BB},k} \in \mathbb{C}^{N_{\text{RF}} \times D_k}$  is the digital precoder corresponding to  $\mathbf{s}_k$  and  $[\mathbf{F}_{\text{BB},1}, \mathbf{F}_{\text{BB},2}, \dots, \mathbf{F}_{\text{BB},K}] = \mathbf{F}_{\text{BB}}$ . Typically, the

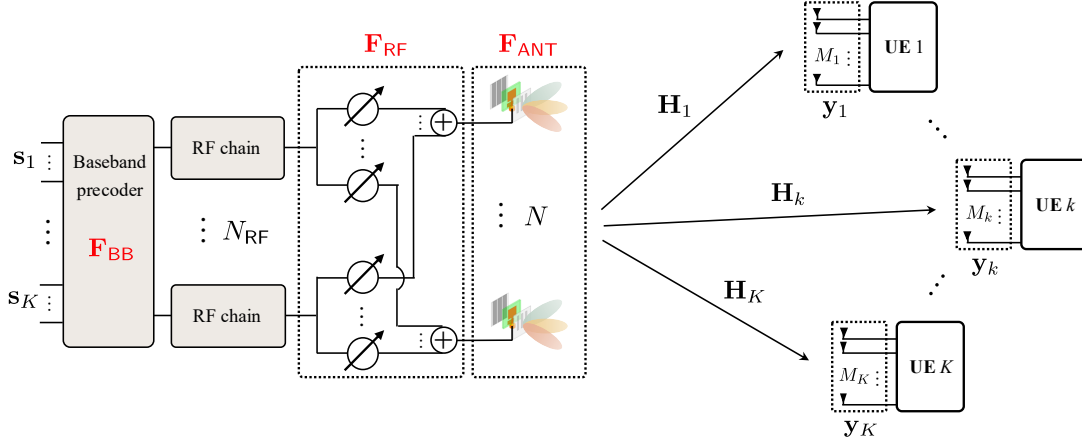


Fig. 1. Illustration of a multi-user MIMO system employing a tri-hybrid precoding architecture at the BS. In addition to digital and analog precoding, the design also incorporates reconfigurable radiation patterns at each transmit antenna. The antenna precoder, denoted as  $\mathbf{F}_{\text{ANT}}$ , will be detailed in Section III. Depending on the adopted model,  $\mathbf{F}_{\text{ANT}}$  may represent either the selection matrix  $\mathbf{F}_{\text{sel}}$  or the coefficient matrix  $\mathbf{F}_{\text{cof}}$ .

analog precoder  $\mathbf{F}_{\text{RF}}$  is implemented with constant modulus, and the digital precoder  $\mathbf{F}_{\text{BB}}$  can be arbitrarily designed within the transmit power constraint. To be clear, this paper assumes each entry of  $\mathbf{F}_{\text{RF}}$  has a constant amplitude, satisfying  $|\mathbf{F}_{\text{RF}}[i,j]|^2 = 1/N, \forall i, j$  [24]–[26]. Further, considering an independent power budget  $P_n$  for the power amplifier at each transmit antenna,  $\forall n$ , this paper adopts a practical per-antenna power constraint, which can be written as [27], [28]

$$[\mathbf{F}_{\text{RF}}\mathbf{F}_{\text{BB}}\mathbf{F}_{\text{BB}}^H\mathbf{F}_{\text{RF}}^H]_{n,n} \leq P_n, \forall n. \quad (2)$$

Let  $\mathbf{H}_k \in \mathbb{C}^{M_k \times N}$  denote the channel from the BS to the  $k^{\text{th}}$  UE. The received signal at the  $k^{\text{th}}$  UE can be expressed as

$$\begin{aligned} \mathbf{y}_k &= \mathbf{H}_k \mathbf{x} + \mathbf{n}_k, \\ &= \mathbf{H}_k \mathbf{F}_{\text{RF}} \mathbf{F}_{\text{BB},k} \mathbf{s}_k + \sum_{i \neq k} \mathbf{H}_k \mathbf{F}_{\text{RF}} \mathbf{F}_{\text{BB},i} \mathbf{s}_i + \mathbf{n}_k, \end{aligned} \quad (3)$$

where the first term is the desired signal for the  $k^{\text{th}}$  UE, the second term is the multi-user interference, and  $\mathbf{n}_k \sim \mathcal{CN}(\mathbf{0}, \sigma_k^2 \mathbf{I})$  is the additive white Gaussian noise at the  $k^{\text{th}}$  UE. Therefore, the spectral efficiency (rate) of the  $k^{\text{th}}$  user is given by [6]

$$\begin{aligned} R_k &= \log_2 \det \left( \mathbf{I}_{M_k} + \mathbf{H}_k \mathbf{F}_{\text{RF}} \mathbf{F}_{\text{BB},k} \mathbf{F}_{\text{BB},k}^H \mathbf{F}_{\text{RF}}^H \mathbf{H}_k^H \right. \\ &\quad \left. \times \left( \sum_{i \neq k} \mathbf{H}_k \mathbf{F}_{\text{RF}} \mathbf{F}_{\text{BB},i} \mathbf{F}_{\text{BB},i}^H \mathbf{F}_{\text{RF}}^H \mathbf{H}_k^H + \sigma_k^2 \mathbf{I}_{M_k} \right)^{-1} \right). \end{aligned} \quad (4)$$

Subsequently, the weighted sum-rate of the entire system is

$$R = \sum_{k=1}^K \beta_k R_k, \quad (5)$$

where  $\beta_k \in \mathbb{R}_+$  is a priority weight for the  $k^{\text{th}}$  user.

In general, the conventional hybrid precoding architecture jointly designs the baseband precoder  $\mathbf{F}_{\text{BB}}$  and the RF precoder  $\mathbf{F}_{\text{RF}}$  to achieve desired signal reception. In this paper, we will demonstrate that the reconfigurability of the transmit antennas introduces additional flexibility in artificially shaping the wireless channels  $\{\mathbf{H}_k\}_{k=1}^K$ . To ensure a thorough understanding, we begin by revisiting the fundamental definitions

of antenna gain and radiation pattern, upon which the detailed expressions of the wireless channels will be built.

## B. Radiation Pattern and Antenna Gain

1) *Radiation Pattern*: An antenna radiation pattern is defined as a mathematical function or a graphical representation of the radiation properties of the antenna as a function of space coordinates. In most cases, the radiation pattern is determined in the far-field region of the radiator and is represented as a function of the directional coordinates (e.g. angle-of-departure (AoD) or angle-of-arrival (AoA)). Radiation properties include power flux density, radiation intensity, field strength, directivity, phase or polarization [29, Ch. 2]. A radiation pattern can be either *magnitude pattern* or *power pattern*.

2) *Antenna Gain*: The antenna gain is defined as the radiation intensity of an antenna in a given direction relative to that of an isotropic radiator [29], [30]. Typically, the antenna gain refers to the radiation *power* intensity relative to an isotropic antenna. Consider a radiator with a total radiated power  $P_{\text{rad}}$ . For an isotropic radiator, its radiation power intensity at any direction  $(\theta, \phi)$  is given by  $U_{\text{iso}}(\theta, \phi) = P_{\text{rad}}/4\pi$  (W/sr). Then, for a general radiator with a radiation power intensity distribution  $U(\theta, \phi)$ , its antenna gain is defined as

$$\text{AG}(\theta, \phi) = \frac{U(\theta, \phi)}{U_{\text{iso}}(\theta, \phi)} = \frac{4\pi U(\theta, \phi)}{P_{\text{rad}}}. \quad (6)$$

In decibels, we have  $\text{AG}_{\text{dBi}}(\theta, \phi) = 10 \log_{10} \text{AG}(\theta, \phi)$  (dBi).

In this paper, we define the *magnitude gain* (or *field gain*) of antennas as

$$G(\theta, \phi) = \sqrt{\text{AG}(\theta, \phi)}. \quad (7)$$

According to the definition of radiation pattern in Section II-B1,  $G(\theta, \phi)$ , as a function of spatial direction, is also a radiation pattern. In this paper, we do not distinguish them. Both antenna radiation pattern and antenna magnitude gain refer to  $G(\theta, \phi)$ . Furthermore, polarization effects are not considered in this study to focus on the tri-hybrid precoding mechanisms enabled by pattern reconfigurability. Future work may incorporate polarization effects to refine channel models.

**Remark 1:** Considering the total radiation power  $P_{\text{rad}}$ , we have

$$\int_0^{2\pi} \int_0^\pi U(\theta, \phi) \sin \theta d\theta d\phi = P_{\text{rad}}. \quad (8)$$

Then, combining (6), (7), and (8) yields

$$\int_0^{2\pi} \int_0^\pi G^2(\theta, \phi) \sin \theta d\theta d\phi = 4\pi. \quad (9)$$

**Remark 2:** The antenna magnitude gain in linear scale must be strictly positive, i.e.,

$$G(\theta, \phi) > 0, \quad \forall (\theta, \phi). \quad (10)$$

However, it may take negative values when expressed in dB.

### C. A General MIMO Channel Model

Based on the defined antenna magnitude gain, we present a general MIMO channel model applicable to both far-field and near-field scenarios, which facilitates subsequent analysis. In a general narrowband multipath MIMO system, the channel matrix  $\mathbf{H}_k$  in the frequency domain can be expressed as

$$\mathbf{H}_k = \sqrt{\frac{NM_k}{L_k}} \sum_{\ell=1}^{L_k} \mathbf{C}_{k,\ell} \odot \mathbf{A}_{k,\ell} \odot \mathbf{G}_{k,\ell}^{\text{UE}} \odot \mathbf{G}_{k,\ell}^{\text{BS}}, \quad (11)$$

where  $L_k$  represents the total number of multipath components between the BS and the  $k^{\text{th}}$  UE,  $\mathbf{C}_{k,\ell} \in \mathbb{C}^{M_k \times N}$  stores the complex channel gains,  $\mathbf{A}_{k,\ell} \in \mathbb{C}^{M_k \times N}$  captures the phase differences among array elements (i.e., the array manifold), and  $\mathbf{G}_{k,\ell}^{\text{UE}}, \mathbf{G}_{k,\ell}^{\text{BS}} \in \mathbb{R}_+^{M_k \times N}$  are the antenna magnitude gain matrices at the  $k^{\text{th}}$  UE and the BS, respectively. Specifically, for the per-antenna link from the  $n^{\text{th}}$  antenna at the BS to the  $m^{\text{th}}$  antenna at the  $k^{\text{th}}$  UE through the  $\ell^{\text{th}}$  path, the complex channel gain, phase difference relative to the reference antennas, transmit antenna magnitude gain, and receive antenna magnitude gain are given by  $[\mathbf{C}_{k,\ell}]_{m,n}$ ,  $[\mathbf{A}_{k,\ell}]_{m,n}$ ,  $[\mathbf{G}_{k,\ell}^{\text{BS}}]_{m,n}$  and  $[\mathbf{G}_{k,\ell}^{\text{UE}}]_{m,n}$ , respectively.

1) *Channel Component Expressions:* A set of commonly used expressions for these components is given by [31]:

$$[\mathbf{C}_{k,\ell}]_{m,n} = \left( \frac{\lambda}{4\pi d_{k,\ell}^{(mn)}} \right)^{\zeta/2} e^{j\psi_{k,\ell}^{(mn)}}, \quad (12a)$$

$$[\mathbf{A}_{k,\ell}]_{m,n} = \frac{1}{\sqrt{NM_k}} e^{-j\frac{2\pi}{\lambda}(d_{k,\ell}^{(mn)} - d_{k,\ell})}, \quad (12b)$$

$$[\mathbf{G}_{k,\ell}^{\text{BS}}]_{m,n} = G_{(n)}^{\text{BS}}(\theta_{k,\ell}^{(mn)}, \phi_{k,\ell}^{(mn)}), \quad (12c)$$

$$[\mathbf{G}_{k,\ell}^{\text{UE}}]_{m,n} = G_{k,(m)}^{\text{UE}}(\vartheta_{k,\ell}^{(mn)}, \varphi_{k,\ell}^{(mn)}), \quad (12d)$$

where  $m = 1, 2, \dots, M_k$ , and  $n = 1, 2, \dots, N$ . Note that we use a parenthesis in the right-hand side expressions to highlight the antenna indices, which will be consistently used throughout the paper. Here,  $\lambda$  is the signal wavelength,  $d_{k,\ell}^{(mn)}$  denote the propagation distance from the  $n^{\text{th}}$  transmit antenna to the  $m^{\text{th}}$  receive antenna through the path  $(k, \ell)$ ,  $\zeta$  is the path loss exponent,  $\psi_{k,\ell}^{(mn)}$  is a random phase shift, and  $d_{k,\ell}$  is the propagation distance between two reference points at the BS and the  $k^{\text{th}}$  UE. In addition, we denote each antenna's magnitude gain as  $G_{(n)}^{\text{BS}}$  or  $G_{k,(m)}^{\text{UE}}$ , which is a function of signal AoD or AoA. Considering a 3D space, we use  $\theta_{k,\ell}^{(mn)}$

and  $\phi_{k,\ell}^{(mn)}$  to respectively denote the inclination and azimuth components of the AoD at the BS, and use  $\vartheta_{k,\ell}^{(mn)}$  and  $\varphi_{k,\ell}^{(mn)}$  to denote that of the AoA at the  $k^{\text{th}}$  UE.

#### 2) Connection to the Conventional Far-Field Model:

While (11) serves as a general yet complex model, we show that it can be simplified and reduce to the conventional model under the far-field assumption. In the far-field, all per-antenna links share the same channel gain  $C_{k,\ell}$ , leading to:

$$\mathbf{C}_{k,\ell} = C_{k,\ell} \mathbf{1}_{M_k \times N}. \quad (13)$$

Additionally, all antennas at the BS/UE share the same AoDs/AoAs, i.e.,  $\theta_{k,\ell}^{(mn)} = \theta_{k,\ell}$ ,  $\phi_{k,\ell}^{(mn)} = \phi_{k,\ell}$ ,  $\vartheta_{k,\ell}^{(mn)} = \vartheta_{k,\ell}$ ,  $\varphi_{k,\ell}^{(mn)} = \varphi_{k,\ell}$ ,  $\forall m, n$ . Furthermore, it is typically assumed that all antennas at the BS and UE exhibit the same fixed radiation pattern, i.e.,  $G_{(n)}^{\text{BS}} = G^{\text{BS}}$ ,  $\forall n$ , and  $G_{k,(m)}^{\text{UE}} = G_k^{\text{UE}}$ ,  $\forall m$ . Consequently, we obtain:

$$\mathbf{G}_{k,\ell}^{\text{UE}} \odot \mathbf{G}_{k,\ell}^{\text{BS}} = G_k^{\text{UE}}(\vartheta_{k,\ell}, \varphi_{k,\ell}) G^{\text{BS}}(\theta_{k,\ell}, \phi_{k,\ell}) \mathbf{1}_{M_k \times N}. \quad (14)$$

The array manifold in the far-field can be decomposed into the rank-one product of two array response vectors (ARVs) as

$$\mathbf{A}_{k,\ell} = \mathbf{a}_{\text{UE}}(\vartheta_{k,\ell}, \varphi_{k,\ell}) \mathbf{a}_{\text{BS}}^{\text{H}}(\theta_{k,\ell}, \phi_{k,\ell}). \quad (15)$$

Assuming the BS an  $N_h \times N_v$  uniform planar array (UPA) configuration (thus  $N = N_h N_v$ ), its far-field ARV is given by

$$\mathbf{a}_{\text{BS}}(\theta_{k,\ell}, \phi_{k,\ell}) = \frac{1}{\sqrt{N}} e^{-j2\pi \varpi_{k,\ell}^h \mathbf{k}(N_h)} \otimes e^{-j2\pi \varpi_{k,\ell}^v \mathbf{k}(N_v)}, \quad (16)$$

where  $\mathbf{k}(n) = [0, 1, \dots, n-1]^{\text{T}}$ , and  $\varpi_{k,\ell}^h$  and  $\varpi_{k,\ell}^v$  are the spatial angles corresponding to the horizontal and vertical dimensions, respectively. Typically,  $\varpi_{k,\ell}^h = d_{\text{BS}} \sin(\phi_{k,\ell}) \sin(\theta_{k,\ell}) / \lambda$  and  $\varpi_{k,\ell}^v = d_{\text{BS}} \cos(\theta_{k,\ell}) / \lambda$ , where  $d_{\text{BS}}$  denotes the inter-element spacing of the antenna array at the BS. The ARV at the UEs is defined analogously.

Substituting (13)–(15) into (11), we obtain the commonly used frequency-domain far-field multipath MIMO channel model as [25], [31]–[33]

$$\mathbf{H}_k = \sqrt{\frac{NM_k}{L_k}} \sum_{\ell=1}^{L_k} C_{k,\ell} G_k^{\text{UE}}(\vartheta_{k,\ell}, \varphi_{k,\ell}) G^{\text{BS}}(\theta_{k,\ell}, \phi_{k,\ell}) \times \mathbf{a}_{\text{UE}}(\vartheta_{k,\ell}, \varphi_{k,\ell}) \mathbf{a}_{\text{BS}}^{\text{H}}(\theta_{k,\ell}, \phi_{k,\ell}). \quad (17)$$

Since (11) is a general model, our subsequent analysis is based on it without differentiating between far-field and near-field scenarios. This paper focuses on tri-hybrid precoding at the BS, while assuming that all UEs are equipped with conventional antennas with fixed radiation patterns. Under this assumption, the reconfigurability of antenna radiation patterns can be captured by modeling the reconfigurable antenna gain in (12c). Following this, two models for pattern-reconfigurable antennas are introduced and discussed in Section III.

### III. INCORPORATING ANTENNA RADIATION PATTERN RECONFIGURABILITY

The reconfigurability of antenna radiation patterns can be modeled using two different approaches. The first is inspired by practical hardware designs, where antennas switch among a finite set of states, each corresponding to a distinct radiation

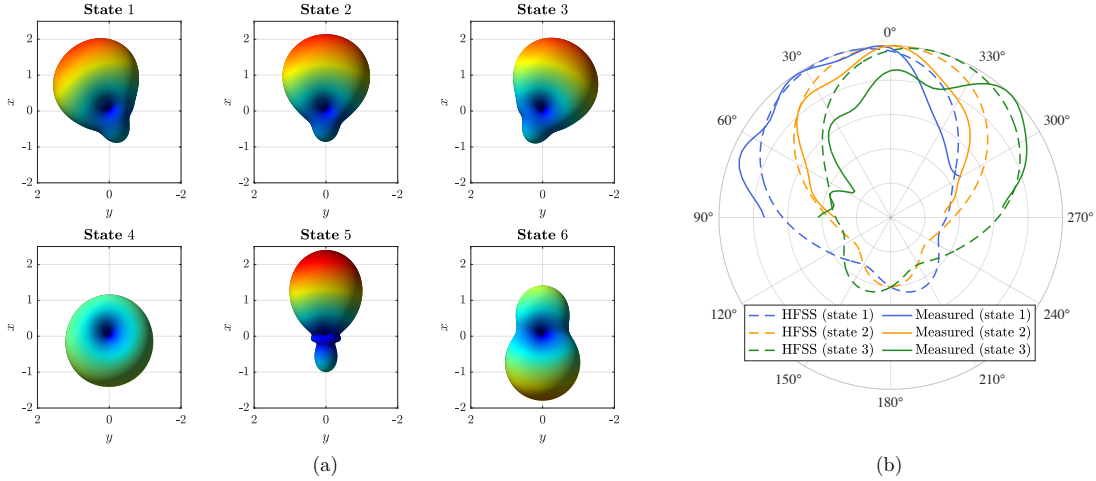


Fig. 2. Illustration of several achievable radiation patterns in the reconfigurable antenna prototype in [22]. (a) Six sample radiation patterns obtained through HFSS full-wave simulations, where the antenna is oriented toward the positive  $x$ -axis. (b) Measured radiation patterns for three states in an anechoic chamber.

pattern. A representative hardware prototype can be found in, e.g., [22]. The second approach considers an idealized antenna capable of generating arbitrary radiation patterns on demand, as studied in [23]. This section presents a separate integration of both models into the MIMO channel (11).

#### A. Model I: Limited State Selection

The limited state selection model offers the most realistic representation, closely aligning with practical hardware designs. Figure 2 illustrates an example of several achievable radiation patterns in a reconfigurable antenna prototype [22]. In general, we can assume a set of  $S$  available radiation pattern candidates, denoted as  $\{\bar{G}_1, \bar{G}_2, \dots, \bar{G}_S\}$ , from which each antenna can select its radiation pattern. Again, each  $\bar{G}_s$  is a function of direction  $(\theta, \phi)$ . For a given angle  $(\theta, \phi)$ , we can define a candidate vector as  $\bar{\mathbf{g}}(\theta, \phi) = [\bar{G}_1(\theta, \phi), \bar{G}_2(\theta, \phi), \dots, \bar{G}_S(\theta, \phi)]^T \in \mathbb{R}_+^S$ . Thus, the radiation pattern of the BS antennas in (12c) can be expressed as

$$G_{(n)}^{\text{BS}}(\theta, \phi) = \bar{\mathbf{g}}^T(\theta, \phi) \mathbf{b}_{(n)}, \quad (18)$$

where  $\mathbf{b}_{(n)}$  is a binary vector denoting the state selection of the  $n^{\text{th}}$  antenna. Specifically, the following constraint applies:

$$\mathbf{b}_{(n)} \in \{\mathbf{b} \in \{0, 1\}^S \mid \|\mathbf{b}\|_0 = 1\}, \quad \forall n. \quad (19)$$

Now, we incorporate expression (18) into (11). We first extend BS antenna magnitude gain matrix  $\bar{\mathbf{G}}_{k,\ell}^{\text{BS}}$  as

$$\bar{\mathbf{G}}_{k,\ell}^{\text{BS}} = \begin{bmatrix} \bar{\mathbf{g}}^T(\theta_{k,\ell}^{(11)}, \phi_{k,\ell}^{(11)}) & \dots & \bar{\mathbf{g}}^T(\theta_{k,\ell}^{(1N)}, \phi_{k,\ell}^{(1N)}) \\ \vdots & \ddots & \vdots \\ \bar{\mathbf{g}}^T(\theta_{k,\ell}^{(M_k 1)}, \phi_{k,\ell}^{(M_k 1)}) & \dots & \bar{\mathbf{g}}^T(\theta_{k,\ell}^{(M_k N)}, \phi_{k,\ell}^{(M_k N)}) \end{bmatrix}, \quad (20)$$

and define a state selection matrix as

$$\mathbf{F}_{\text{sel}} = \text{blkdiag}\{\mathbf{b}_{(1)}, \mathbf{b}_{(2)}, \dots, \mathbf{b}_{(N)}\}, \quad (21)$$

where  $\text{blkdiag}$  denotes the block diagonal operator that constructs a block diagonal matrix from its vector inputs. Note

that  $\bar{\mathbf{G}}_{k,\ell}^{\text{BS}} \in \mathbb{R}_+^{M_k \times NS}$  and  $\mathbf{F}_{\text{sel}} \in \{0, 1\}^{NS \times N}$ . Subsequently, channel model (11) can be rewritten as

$$\mathbf{H}_k = \mathbf{H}_k^{\text{sel}} \mathbf{F}_{\text{sel}}, \quad (22)$$

where the effective channel  $\mathbf{H}_k^{\text{sel}}$  is defined as

$$\mathbf{H}_k^{\text{sel}} \triangleq \sqrt{\frac{NM_k}{L_k}} \sum_{\ell=1}^{L_k} \left( (\mathbf{C}_{k,\ell} \odot \mathbf{A}_{k,\ell} \odot \mathbf{G}_{k,\ell}^{\text{UE}}) \otimes \mathbf{1}_{1 \times S} \right) \odot \bar{\mathbf{G}}_{k,\ell}^{\text{BS}} \in \mathbb{C}^{M_k \times NS}, \quad (23)$$

Substituting (22) into (3) yields the tri-hybrid signal model based on the limited state selection mechanism as:

$$\mathbf{y}_k = \mathbf{H}_k^{\text{sel}} \mathbf{F}_{\text{sel}} \mathbf{F}_{\text{RF}} \mathbf{F}_{\text{BB},k} \mathbf{s}_k + \sum_{i \neq k} \mathbf{H}_k^{\text{sel}} \mathbf{F}_{\text{sel}} \mathbf{F}_{\text{RF}} \mathbf{F}_{\text{BB},i} \mathbf{s}_i + \mathbf{n}_k.$$

This model enables the joint adjustment of  $\{\mathbf{F}_{\text{sel}}, \mathbf{F}_{\text{RF}}, \mathbf{F}_{\text{BB}}\}$  to achieve the desired signal receptions.

#### B. Model II: Arbitrary Radiation Pattern Generation

Apart from the limited state selection model, an alternative approach models pattern-reconfigurable antennas as capable of generating arbitrary radiation patterns. While this assumption may be overly idealized, it reveals the ultimate potential of such antennas, as it represents the upper-bound performance achievable. Moreover, future advancements in antenna design and fabrication may make this idealized performance attainable. Some preliminary explorations on orthogonal antenna pattern generation already exist; see, e.g., [34].

A radiation pattern can be equivalently represented either in the angular domain [23] or in the spherical domain [17]. Typically, the angular domain representation results in a much heavier effective channel matrix, whereas the spherical domain allows for a more compact characterization of the radiation pattern using fewer coefficients due to the band-limited nature of most practical radiation patterns [21], [35]. For this reason, this paper adopts the spherical domain representation. Based on spherical harmonics decomposition, any radiation pattern

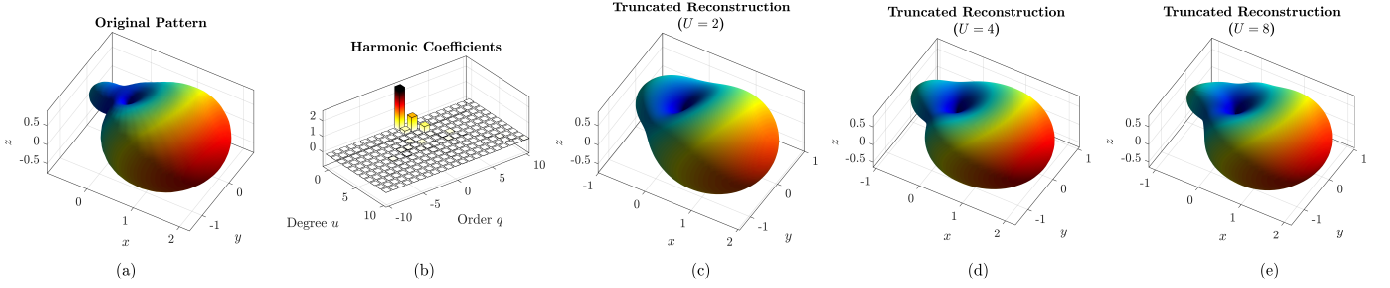


Fig. 3. Illustration of spherical harmonics decomposition and truncated reconstruction. (a) An HFSS simulated radiation pattern for a selected state of the reconfigurable antenna design in [22]. (b) Visualization of its spherical harmonic coefficients, showing the dominance of low-degree coefficients, which justifies the truncation operation. (c) Truncated reconstruction with  $U = 2$ . (d) Truncated reconstruction with  $U = 4$ . (e) Truncated reconstruction with  $U = 8$ .

can be expressed as a superposition of an infinite series of spherical harmonics as

$$G_{(n)}^{\text{BS}}(\theta, \phi) = \sum_{u=0}^{+\infty} \sum_{q=-u}^u c_{uq}^{(n)} Y_u^q(\theta, \phi). \quad (24)$$

Here,  $c_{uq}^{(n)}$  denotes the harmonic coefficient and  $Y_u^q(\theta, \phi)$  is the *real* spherical harmonics defined as

$$Y_u^q(\theta, \phi) = \begin{cases} \sqrt{2} N_u^q P_u^q(\cos \theta) \cos(q\phi), & q > 0, \\ \sqrt{2} N_u^{|q|} P_u^{|q|}(\cos \theta) \sin(|q|\phi), & q < 0, \\ N_u^0 P_u^0(\cos \theta), & q = 0, \end{cases} \quad (25)$$

where  $N_u^q = \sqrt{\frac{2u+1}{4\pi} \frac{(u-q)!}{(u+q)!}}$  is a normalization factor, and  $P_u^q(\cos \theta)$  represents the associated Legendre functions of  $u^{\text{th}}$  degree and  $q^{\text{th}}$  order. This set of functions  $Y_u^q(\theta, \phi)$  constitutes a complete real orthonormal basis on the spherical space.

We further apply a truncation to (24). By defining the truncation length  $T = U^2 + 2U + 1$ , we can approximate the radiation pattern of the  $n^{\text{th}}$  antenna as

$$G_{(n)}^{\text{BS}}(\theta, \phi) \approx \sum_{u=0}^U \sum_{q=-u}^u c_{uq}^{(n)} Y_u^q(\theta, \phi) = \sum_{t=1}^T \tilde{c}_t^{(n)} \tilde{Y}_t(\theta, \phi), \quad (26)$$

where  $\tilde{c}_t^{(n)} = c_{uq}^{(n)}$  and  $\tilde{Y}_t(\theta, \phi) = Y_u^q(\theta, \phi)$ , for  $t = u^2 + u + q + 1$ ,  $u \in [0, U]$ ,  $q \in [-u, u]$ . For convenience, we further concatenate  $\mathbf{c}_{(n)} \triangleq [\tilde{c}_1^{(n)}, \tilde{c}_2^{(n)}, \dots, \tilde{c}_T^{(n)}]^{\text{T}} \in \mathbb{R}^T$ ,  $\boldsymbol{\gamma}(\theta, \phi) \triangleq [\tilde{Y}_1(\theta, \phi), \tilde{Y}_2(\theta, \phi), \dots, \tilde{Y}_T(\theta, \phi)]^{\text{T}} \in \mathbb{R}^T$ , where  $\mathbf{c}_{(n)}$  is the coefficient vector of the  $n^{\text{th}}$  antenna element, and  $\boldsymbol{\gamma}(\theta, \phi)$  is the spherical basis vector. Then, we can rewrite (24) as

$$G_{(n)}^{\text{BS}}(\theta, \phi) \approx \boldsymbol{\gamma}^{\text{T}}(\theta, \phi) \mathbf{c}_{(n)}. \quad (27)$$

Based on (9) and the energy conservation law in spherical harmonics transform, we have the following constraint:

$$\|\mathbf{c}_{(n)}\|_2^2 = 4\pi, \quad \forall n. \quad (28)$$

An example of spherical harmonics decomposition and the truncated reconstruction is illustrated in Fig. 3. Additionally, we note that (27) has the same form as (18) in Model I. Actually, the  $4\pi$  factor is also included in Model I. Each candidate pattern in  $\bar{\mathbf{g}}(\theta, \phi)$ , i.e.,  $\bar{G}_s(\theta, \phi)$ , has a total power  $\int_0^{2\pi} \int_0^\pi \bar{G}_s^2(\theta, \phi) \sin \theta d\theta d\phi = 4\pi$ , according to Remark 1.

Similarly, we can define a harmonics coefficient matrix as

$$\mathbf{F}_{\text{cof}} = \text{blkdiag}\{\mathbf{c}_{(1)}, \mathbf{c}_{(2)}, \dots, \mathbf{c}_{(N)}\}, \quad (29)$$

and an extended BS antenna radiation pattern basis matrix as

$$\mathbf{\Gamma}_{k,\ell}^{\text{BS}} = \begin{bmatrix} \boldsymbol{\gamma}^{\text{T}}(\theta_{k,\ell}^{(11)}, \phi_{k,\ell}^{(11)}) & \dots & \boldsymbol{\gamma}^{\text{T}}(\theta_{k,\ell}^{(1N)}, \phi_{k,\ell}^{(1N)}) \\ \vdots & \ddots & \vdots \\ \boldsymbol{\gamma}^{\text{T}}(\theta_{k,\ell}^{(M_k 1)}, \phi_{k,\ell}^{(M_k 1)}) & \dots & \boldsymbol{\gamma}^{\text{T}}(\theta_{k,\ell}^{(M_k N)}, \phi_{k,\ell}^{(M_k N)}) \end{bmatrix}. \quad (30)$$

Note that  $\mathbf{F}_{\text{cof}} \in \mathbb{R}^{NT \times N}$  and  $\mathbf{\Gamma}_{k,\ell}^{\text{BS}} \in \mathbb{R}^{M_k \times NT}$ . Then, the effective channel  $\mathbf{H}_k^{\text{cof}}$  can be obtained as

$$\mathbf{H}_k^{\text{cof}} \triangleq \sqrt{\frac{NM_k}{L_k}} \sum_{\ell=1}^{L_k} \left( (\mathbf{C}_{k,\ell} \odot \mathbf{A}_{k,\ell} \odot \mathbf{G}_{k,\ell}^{\text{UE}}) \otimes \mathbf{1}_{1 \times T} \right) \odot \mathbf{\Gamma}_{k,\ell}^{\text{BS}} \in \mathbb{C}^{M_k \times NT}. \quad (31)$$

Finally, we have a similar channel expression as

$$\mathbf{H}_k = \mathbf{H}_k^{\text{cof}} \mathbf{F}_{\text{cof}}. \quad (32)$$

Substituting (32) into (3) yields the other tri-hybrid signal model as

$$\mathbf{y}_k = \mathbf{H}_k^{\text{cof}} \mathbf{F}_{\text{cof}} \mathbf{F}_{\text{RF}} \mathbf{F}_{\text{BB},k} \mathbf{s}_k + \sum_{i \neq k} \mathbf{H}_k^{\text{cof}} \mathbf{F}_{\text{cof}} \mathbf{F}_{\text{RF}} \mathbf{F}_{\text{BB},i} \mathbf{s}_i + \mathbf{n}_k.$$

### C. Comparison Between the Two Models

Now, we have obtained two models,  $\{\mathbf{H}_k^{\text{sel}}, \mathbf{F}_{\text{sel}}\}$  and  $\{\mathbf{H}_k^{\text{cof}}, \mathbf{F}_{\text{cof}}\}$ , to characterize the radiation pattern reconfigurability of the antennas at the BS. The key differences between these models can be summarized as follows:

- **Different physical interpretations:** Model I represents the antenna state selection, where  $\mathbf{F}_{\text{sel}}$  denotes the state selection of the BS antennas, and  $\mathbf{H}_k^{\text{sel}}$  integrates all possible channels based on the available radiation pattern candidates. In contrast, Model II models arbitrary radiation pattern synthesis, where  $\mathbf{F}_{\text{cof}}$  represents the spherical harmonic coefficients, and  $\mathbf{H}_k^{\text{cof}}$  is a concatenation of channels based on each spherical basis.
- **Different matrix dimensions:** Both models introduce a dimensional lift to the channels. The original channel is  $\mathbf{H}_k \in \mathbb{C}^{M_k \times N}$ , the effective channel in Model I is  $\mathbf{H}_k^{\text{sel}} \in \mathbb{C}^{M_k \times NS}$ , while the effective channel in Model II is  $\mathbf{H}_k^{\text{cof}} \in \mathbb{C}^{M_k \times NT}$ . Here,  $S$  denotes the total number of available antenna states, and  $T$  represents the truncation length of the spherical harmonics decomposition.
- **Different constraints:** While both  $\mathbf{F}_{\text{sel}}$  and  $\mathbf{F}_{\text{cof}}$  exhibit a similar block diagonal structure, as shown

in (21) and (29), they impose different constraints. Each diagonal block in  $\mathbf{F}_{\text{sel}}$  is constrained as  $\mathbf{b}_{(n)} \in \{\mathbf{b} \in \{0, 1\}^S \mid \|\mathbf{b}\|_0 = 1\}$ , whereas in  $\mathbf{F}_{\text{cof}}$ , the constraint is  $\|\mathbf{c}_{(n)}\|_2^2 = 4\pi$ , as shown in (19) and (28), respectively. The constraint difference significantly affects the optimization algorithm design. We observe that while Model II is less practical, its constraint is milder, meaning that it is often easier to optimize compared to Model I.

#### IV. TRI-HYBRID PRECODING BASED ON MODEL I

Based on Model I, the considered tri-hybrid precoding problem aims to optimize  $\{\mathbf{F}_{\text{sel}}, \mathbf{F}_{\text{RF}}, \mathbf{F}_{\text{BB}}\}$  jointly to maximize the weighted sum-rate defined in (5). We assume perfect knowledge of the effective channel  $\mathbf{H}_k^{\text{sel}}, \forall k$ . To simplify the optimization, we temporarily define a fully digital precoder  $\mathbf{F}_{\text{D}} \triangleq \mathbf{F}_{\text{RF}}\mathbf{F}_{\text{BB}} \in \mathbb{C}^{N \times D}$ , and seek the optimal solution of the reduced set  $\{\mathbf{F}_{\text{sel}}, \mathbf{F}_{\text{D}}\}$  instead. The optimized  $\mathbf{F}_{\text{D}}$  is then decomposed back into  $\mathbf{F}_{\text{RF}}$  and  $\mathbf{F}_{\text{BB}}$ . Partitioning  $\mathbf{F}_{\text{D}} = [\mathbf{F}_{\text{D},1}, \mathbf{F}_{\text{D},2}, \dots, \mathbf{F}_{\text{D},K}]$ , where  $\mathbf{F}_{\text{D},k} \in \mathbb{C}^{N \times D_k}$ , we formulate the initial precoding problem as:

$$\max_{\mathbf{F}_{\text{sel}}, \mathbf{F}_{\text{D}}} \sum_{k=1}^K \beta_k \log_2 \det \left( \mathbf{I}_{M_k} + \mathbf{H}_k^{\text{sel}} \mathbf{F}_{\text{sel}} \mathbf{F}_{\text{D},k} \mathbf{F}_{\text{D},k}^{\text{H}} \mathbf{F}_{\text{sel}}^{\text{H}} (\mathbf{H}_k^{\text{sel}})^{\text{H}} \right) \times \left( \sum_{i \neq k} \mathbf{H}_k^{\text{sel}} \mathbf{F}_{\text{sel}} \mathbf{F}_{\text{D},i} \mathbf{F}_{\text{D},i}^{\text{H}} \mathbf{F}_{\text{sel}}^{\text{H}} (\mathbf{H}_k^{\text{sel}})^{\text{H}} + \sigma_k^2 \mathbf{I}_{M_k} \right)^{-1} \quad (33a)$$

$$\text{s.t. } [\mathbf{F}_{\text{D}} \mathbf{F}_{\text{D}}^{\text{H}}]_{n,n} \leq P_n, \quad \forall n, \quad (33b)$$

$$\mathbf{F}_{\text{sel}} = \text{blkdiag}\{\mathbf{b}_{(1)}, \mathbf{b}_{(2)}, \dots, \mathbf{b}_{(N)}\}, \quad (33c)$$

$$\mathbf{b}_{(n)} \in \{\mathbf{b} \in \{0, 1\}^S \mid \|\mathbf{b}\|_0 = 1\}, \quad \forall n. \quad (33d)$$

##### A. Conversion to the Weighted Sum MSE Minimization

According to [28], [36], the formulated weighted sum-rate maximization problem is equivalent to a WMMSE minimization problem. Specifically, by applying Lemma 1 in [28], the maximization problem (33) can be recast as the following minimization problem:

$$\min_{\mathbf{W}, \mathbf{U}, \mathbf{F}_{\text{sel}}, \mathbf{F}_{\text{D}}} \sum_{k=1}^K \beta_k (\text{Tr}(\mathbf{W}_k \mathbf{E}_k) - \ln \det(\mathbf{W}_k)) \quad (34a)$$

$$\text{s.t. } [\mathbf{F}_{\text{D}} \mathbf{F}_{\text{D}}^{\text{H}}]_{n,n} \leq P_n, \quad \forall n, \quad (34b)$$

$$\mathbf{F}_{\text{sel}} = \text{blkdiag}\{\mathbf{b}_{(1)}, \mathbf{b}_{(2)}, \dots, \mathbf{b}_{(N)}\}, \quad (34c)$$

$$\mathbf{b}_{(n)} \in \{\mathbf{b} \in \{0, 1\}^S \mid \|\mathbf{b}\|_0 = 1\}, \quad \forall n. \quad (34d)$$

where

$$\mathbf{E}_k \triangleq (\mathbf{I} - \mathbf{U}_k^{\text{H}} \mathbf{H}_k^{\text{sel}} \mathbf{F}_{\text{sel}} \mathbf{F}_{\text{D},k}) (\mathbf{I} - \mathbf{U}_k^{\text{H}} \mathbf{H}_k^{\text{sel}} \mathbf{F}_{\text{sel}} \mathbf{F}_{\text{D},k})^{\text{H}} + \mathbf{U}_k^{\text{H}} \left( \sum_{i \neq k} \mathbf{H}_k^{\text{sel}} \mathbf{F}_{\text{sel}} \mathbf{F}_{\text{D},i} \mathbf{F}_{\text{D},i}^{\text{H}} \mathbf{F}_{\text{sel}}^{\text{H}} (\mathbf{H}_k^{\text{sel}})^{\text{H}} + \sigma_k^2 \mathbf{I} \right) \mathbf{U}_k. \quad (35)$$

Here,  $\mathbf{W} = \{\mathbf{W}_k \in \mathbb{C}^{D_k \times D_k}\}_{k=1}^K$  and  $\mathbf{U} = \{\mathbf{U}_k \in \mathbb{C}^{M_k \times D_k}\}_{k=1}^K$  are two sets of auxiliary variables, with an additional constraint  $\mathbf{W}_k \succ \mathbf{0}, \forall k$ .

Problem (34) can be solved using the block coordinate descent (BCD) method [37]. Although (34) introduces additional optimization variables, the subproblems with respect to each auxiliary variable in  $\{\mathbf{W}, \mathbf{U}\}$  are individually convex

and admit closed-form solutions. As a result, the overall complexity is not significantly increased, while the objective function becomes more tractable compared to the original formulation in (33). According to Lemma 1 in [28], the optimal  $\{\mathbf{W}, \mathbf{U}\}$  are given by

$$\mathbf{U}_k^{\text{opt}} = \left( \sum_{i=1}^K \mathbf{H}_k \mathbf{F}_{\text{D},i} \mathbf{F}_{\text{D},i}^{\text{H}} \mathbf{H}_k^{\text{H}} + \sigma_k^2 \mathbf{I} \right)^{-1} \mathbf{H}_k \mathbf{F}_{\text{D},k}, \quad \forall k, \quad (36)$$

$$\mathbf{W}_k^{\text{opt}} = (\mathbf{I} - (\mathbf{U}_k^{\text{opt}})^{\text{H}} \mathbf{H}_k \mathbf{F}_{\text{D},k})^{-1}, \quad \forall k, \quad (37)$$

with  $\mathbf{H}_k = \mathbf{H}_k^{\text{sel}} \mathbf{F}_{\text{sel}}$ .

##### B. Per-Antenna Optimization of $\mathbf{F}_{\text{sel}}$ and $\mathbf{F}_{\text{D}}$

Now we focus on the optimization of  $\{\mathbf{F}_{\text{sel}}, \mathbf{F}_{\text{D}}\}$  in (34). Considering the per-antenna power constraint (34b) and the per-antenna state selection constraint (34d), we can naturally treat the variables related to each antenna as a block variable and update each antenna alternately, as implemented in [28, Sec. V]. To do so, we first conduct a partition to  $\mathbf{F}_{\text{D}}$  as follows:

$$\mathbf{F}_{\text{D}} = [\mathbf{F}_{\text{D},1} \quad \dots \quad \mathbf{F}_{\text{D},k} \quad \dots \quad \mathbf{F}_{\text{D},K}] \in \mathbb{C}^{N \times D}, \quad (38)$$

$$= \begin{bmatrix} \mathbf{f}_{(1),1}^{\text{H}} & \dots & \mathbf{f}_{(1),k}^{\text{H}} & \dots & \mathbf{f}_{(1),K}^{\text{H}} \\ \vdots & \ddots & \vdots & \ddots & \vdots \\ \mathbf{f}_{(N),1}^{\text{H}} & \dots & \mathbf{f}_{(N),k}^{\text{H}} & \dots & \mathbf{f}_{(N),K}^{\text{H}} \end{bmatrix} = \begin{bmatrix} \mathbf{f}_{(1)}^{\text{H}} \\ \vdots \\ \mathbf{f}_{(N)}^{\text{H}} \end{bmatrix},$$

where  $\mathbf{f}_{(n),k} \in \mathbb{C}^{D_k}$  and  $\mathbf{f}_{(n)} \in \mathbb{C}^D$ . Again  $D = \sum_{k=1}^K D_k$ . Then, we consider the optimization of  $\{\mathbf{f}_{(n)}, \mathbf{b}_{(n)}\}$  given  $\{\mathbf{f}_{(i)}, \mathbf{b}_{(i)}\}_{i \neq n}, \mathbf{U}_k$ , and  $\mathbf{W}_k$ .

The per-antenna optimization problem is written as

$$\min_{\mathbf{f}_{(n)}, \mathbf{b}_{(n)}} \sum_{k=1}^K \beta_k (\text{Tr}(\mathbf{W}_k \mathbf{E}_k) - \ln \det(\mathbf{W}_k)) \quad (39a)$$

$$\text{s.t. } \|\mathbf{f}_{(n)}\|_2^2 \leq P_n, \quad (39b)$$

$$\mathbf{b}_{(n)} \in \{\mathbf{b} \in \{0, 1\}^S \mid \|\mathbf{b}\|_0 = 1\}. \quad (39c)$$

By further partitioning  $\mathbf{H}_k^{\text{sel}} = [\mathbf{H}_{(1),k}^{\text{sel}}, \dots, \mathbf{H}_{(N),k}^{\text{sel}}] \in \mathbb{C}^{M_k \times NS}$ , where  $\mathbf{H}_{(n),k}^{\text{sel}} \in \mathbb{C}^{M_k \times S}$ , we can express

$$\mathbf{H}_k^{\text{sel}} \mathbf{F}_{\text{sel}} \mathbf{F}_{\text{D},i} = \sum_{n=1}^N \mathbf{H}_{(n),k}^{\text{sel}} \mathbf{b}_{(n)} \mathbf{f}_{(n),i}^{\text{H}}, \quad (40)$$

based on which the following Lemma 1 follows.

**Lemma 1:** Optimization problem (39) is equivalent to:

$$\min_{\mathbf{f}_{(n)}, \mathbf{b}_{(n)}} \|\mathbf{f}_{(n)}\|_2^2 \mathbf{b}_{(n)}^{\text{T}} \mathbf{B}_{nn} \mathbf{b}_{(n)} + 2\text{Re} \left( \mathbf{f}_{(n)}^{\text{H}} (\mathbf{Q}_n - \mathbf{D}_n) \mathbf{b}_{(n)} \right)$$

$$\text{s.t. } \|\mathbf{f}_{(n)}\|_2^2 \leq P_n, \quad (41a)$$

$$\mathbf{b}_{(n)} \in \{\mathbf{b} \in \{0, 1\}^S \mid \|\mathbf{b}\|_0 = 1\}, \quad (41b)$$

where

$$\mathbf{B}_{qp} = \sum_{k=1}^K \beta_k (\mathbf{H}_{(q),k}^{\text{sel}})^{\text{H}} \mathbf{U}_k \mathbf{W}_k \mathbf{U}_k^{\text{H}} \mathbf{H}_{(p),k}^{\text{sel}} \in \mathbb{C}^{S \times S}, \quad (42)$$

$$\mathbf{Q}_n = \sum_{q \neq n} \mathbf{f}_{(q)} \mathbf{b}_{(q)}^{\text{T}} \mathbf{B}_{qn} \in \mathbb{C}^{D \times S}, \quad (43)$$

$$\mathbf{D}_n = \begin{bmatrix} \beta_1 \mathbf{W}_1 \mathbf{U}_1^{\text{H}} \mathbf{H}_{(n),1}^{\text{sel}} \\ \vdots \\ \beta_K \mathbf{W}_K \mathbf{U}_K^{\text{H}} \mathbf{H}_{(n),K}^{\text{sel}} \end{bmatrix} \in \mathbb{C}^{D \times S}. \quad (44)$$

**Proof:** This can be proved by substituting (40) into (35) and (39a) while omitting all constant terms.  $\square$

Considering the state selection constraint in (41b), the optimization variable  $\mathbf{b}_{(n)}$  admits only  $S$  possible configurations. Therefore, an enumeration approach can be employed. For each candidate  $\mathbf{b}_{(n)}$ , the corresponding optimal  $\mathbf{f}_{(n)}$  can be derived in closed form. Hence, the global optimum of (41) can be obtained by evaluating and comparing all closed-form solutions of  $\mathbf{f}_{(n)}$  across the  $S$  configurations of  $\mathbf{b}_{(n)}$ .

**Proposition 1:** The optimal solution of (39) can be determined by applying an exhaustive search to  $\mathbf{b}_{(n)} \in \{\mathbf{b} \in \{0, 1\}^S \mid \|\mathbf{b}\|_0 = 1\}$ . Given a candidate  $\mathbf{b}_{(n)}$ , the corresponding optimal  $\mathbf{f}_{(n)}$  is determined as

$$\mathbf{f}_{(n)}^{\text{opt}} = \min \left( \frac{(\mathbf{D}_n - \mathbf{Q}_n)\mathbf{b}_{(n)}}{\mathbf{b}_{(n)}^\top \mathbf{B}_{nn} \mathbf{b}_{(n)}}, \frac{\sqrt{P_n}(\mathbf{D}_n - \mathbf{Q}_n)\mathbf{b}_{(n)}}{\|(\mathbf{Q}_n - \mathbf{D}_n)\mathbf{b}_{(n)}\|_2} \right). \quad (45)$$

**Proof:** See Appendix.  $\square$

### C. Decomposition of $\mathbf{F}_D$ into $\mathbf{F}_{\text{RF}}$ and $\mathbf{F}_{\text{BB}}$

When obtained  $\{\mathbf{f}_{(n)}^{\text{opt}}, \mathbf{b}_{(n)}^{\text{opt}}\}_{n=1}^N$ , we can recover  $\mathbf{F}_{\text{sel}}^{\text{opt}}$  and  $\mathbf{F}_D^{\text{opt}}$  according to (21) and (38), respectively. A final step is to decompose  $\mathbf{F}_D^{\text{opt}}$  back into  $\mathbf{F}_{\text{RF}}^{\text{opt}}$  and  $\mathbf{F}_{\text{BB}}^{\text{opt}}$  by solving the following minimization problem:

$$\min_{\mathbf{F}_{\text{RF}}, \mathbf{F}_{\text{BB}}} \|\mathbf{F}_D^{\text{opt}} - \mathbf{F}_{\text{RF}} \mathbf{F}_{\text{BB}}\|_F^2 \quad (46a)$$

$$\text{s.t.} \quad |[\mathbf{F}_{\text{RF}}]_{i,j}|^2 = 1/N, \quad \forall i, j, \quad (46b)$$

$$[\mathbf{F}_{\text{RF}} \mathbf{F}_{\text{BB}} \mathbf{F}_{\text{BB}}^H \mathbf{F}_{\text{RF}}^H]_{n,n} \leq P_n, \quad \forall n. \quad (46c)$$

Regardless of the per-antenna power constraints (46c), various methods have been proposed to address this decomposition problem (see, e.g., [26], [38]). Based on this, a straightforward approach to solve (46) is to first relax the per-antenna power constraint (46c) to a total power constraint of the form  $\text{Tr}(\mathbf{F}_{\text{RF}} \mathbf{F}_{\text{BB}} \mathbf{F}_{\text{BB}}^H \mathbf{F}_{\text{RF}}^H) \leq \text{Tr}(\mathbf{F}_D^{\text{opt}} (\mathbf{F}_D^{\text{opt}})^H)$ . Then, an existing decomposition algorithm (such as Algorithm 1 in [26]) can be applied to obtain an initial solution  $\tilde{\mathbf{F}}_{\text{RF}}^{\text{opt}}$  and  $\tilde{\mathbf{F}}_{\text{BB}}^{\text{opt}}$ . Next, to enforce the per-antenna power constraint (46c), a normalization step can be performed on the baseband precoder as follows:

$$\mathbf{F}_{\text{BB}}^{\text{opt}} = \tilde{\mathbf{F}}_{\text{BB}}^{\text{opt}} \min_n \left( 1, \sqrt{\frac{P_n}{[\tilde{\mathbf{F}}_{\text{RF}}^{\text{opt}} \tilde{\mathbf{F}}_{\text{BB}}^{\text{opt}} (\tilde{\mathbf{F}}_{\text{BB}}^{\text{opt}})^H (\tilde{\mathbf{F}}_{\text{RF}}^{\text{opt}})^H]_{n,n}}} \right), \quad (47)$$

while keeping  $\mathbf{F}_{\text{RF}}^{\text{opt}} = \tilde{\mathbf{F}}_{\text{RF}}^{\text{opt}}$  unchanged.

### D. Algorithm Summary and Complexity Analysis

As a result, the proposed tri-hybrid precoding algorithm based on Model I is summarized in Algorithm 1.

The computational complexity of Algorithm 1 is analyzed as follows. We consider a massive MIMO system where  $N \gg \sum_{k=1}^K M_k > D > K$ , and thus focus on the complexity with respect to the number of BS antennas  $N$  and the number of available antenna states  $S$ . The complexity of lines 4–6 is dominated by line 4, which has a complexity of  $\mathcal{O}(N^2 S)$ . The operation in line 8 executed over the loop in line 7 incurs a total complexity of  $\mathcal{O}(N S^2)$ , while the updates in lines 9–12 over the loop in line 7 contribute a

### Algorithm 1 Tyi-Hybrid Precoding Based on Model I

- 1: **Input:**  $\mathbf{H}_k^{\text{sel}}, \sigma_k^2, \forall k$ .     **Output:**  $\mathbf{F}_{\text{sel}}^{\text{opt}}, \mathbf{F}_{\text{RF}}^{\text{opt}}, \mathbf{F}_{\text{BB}}^{\text{opt}}$ .
- 2: Initialize  $\mathbf{F}_{\text{sel}}, \mathbf{F}_{\text{RF}}, \mathbf{F}_{\text{BB}}, \mathbf{F}_D = \mathbf{F}_{\text{RF}} \mathbf{F}_{\text{BB}}, \mathbf{W}_k = \mathbf{I}$ , and the maximum iteration number  $I_{\text{max}}$ .
- 3: **for** Iter = 1, 2, ...,  $I_{\text{max}}$  **do**
- 4:     Compute  $\mathbf{H}_k = \mathbf{H}_k^{\text{sel}} \mathbf{F}_{\text{sel}}, \forall k$ .
- 5:     Update  $\mathbf{U}_k = \mathbf{U}_k^{\text{opt}}, \forall k$ , according to (36).
- 6:     Update  $\mathbf{W}_k = \mathbf{W}_k^{\text{opt}}, \forall k$ , according to (37).
- 7:     **for**  $n = 1, 2, \dots, N$  **do**
- 8:         Compute  $\{\mathbf{B}_{nn}, \mathbf{Q}_n, \mathbf{D}_n\}$  according to (42)–(44).
- 9:         **for**  $s = 1, 2, \dots, S$  **do**
- 10:             Let  $\mathbf{b}_{(n)} = \mathbf{0}_{S \times 1}$  and assign  $[\mathbf{b}_{(n)}]_s = 1$ .
- 11:             Compute the optimal  $\mathbf{f}_{(n)}^{\text{opt}}$  given  $\mathbf{b}_{(n)}$  via (45).
- 12:             **end for**
- 13:         Determine the optimal  $\mathbf{b}_{(n)}^{\text{opt}}$  and the corresponding  $\mathbf{f}_{(n)}^{\text{opt}}$  that maximize the objective function in (41).
- 14:     **end for**
- 15:     Recover  $\mathbf{F}_{\text{sel}}^{\text{opt}}$  and  $\mathbf{F}_D^{\text{opt}}$  based on  $\{\mathbf{f}_{(n)}^{\text{opt}}, \mathbf{b}_{(n)}^{\text{opt}}\}_{n=1}^N$  using (21) and (38), respectively.
- 16: **end for**
- 17: Decompose  $\mathbf{F}_D^{\text{opt}}$  back into  $\mathbf{F}_{\text{RF}}^{\text{opt}}$  and  $\mathbf{F}_{\text{BB}}^{\text{opt}}$  using the method described in Section IV-C.

total complexity of  $\mathcal{O}(N S^3)$ . Additionally, the decomposition method in line 17 has a complexity of  $\mathcal{O}(N_{\text{RF}}^2 N + N_{\text{RF}} N D)$  when Algorithm 1 in [26] is adopted. Since  $N_{\text{RF}} > D$ , the overall complexity of Algorithm 1 can be summarized as  $\mathcal{O}(I_{\text{max}}(N^2 S + N S^3 + N_{\text{RF}}^2 N))$ , where  $I_{\text{max}}$  denotes the maximum number of iterations.

## V. TRI-HYBRID PRECODING BASED ON MODEL II

The tri-hybrid precoding based on Model II can be addressed by slightly modifying the approach proposed in Section IV. Specifically, we continue to apply the WMMSE principle to reformulate the optimization problem—now with a different constraint—as follows:

$$\min_{\mathbf{W}, \mathbf{U}, \mathbf{F}_{\text{cof}}, \mathbf{F}_D} \sum_{k=1}^K \beta_k (\text{Tr}(\mathbf{W}_k \mathbf{E}_k) - \ln \det(\mathbf{W}_k)) \quad (48a)$$

$$\text{s.t.} \quad [\mathbf{F}_D \mathbf{F}_D^H]_{n,n} \leq P_n, \quad \forall n, \quad (48b)$$

$$\mathbf{F}_{\text{cof}} = \text{blkdiag}\{\mathbf{c}_{(1)}, \mathbf{c}_{(2)}, \dots, \mathbf{c}_{(N)}\}, \quad (48c)$$

$$\|\mathbf{c}_{(n)}\|_2^2 = 4\pi, \quad \forall n. \quad (48d)$$

where

$$\mathbf{E}_k \triangleq (\mathbf{I} - \mathbf{U}_k^H \mathbf{H}_k^{\text{cof}} \mathbf{F}_{\text{cof}} \mathbf{F}_{D,k}) (\mathbf{I} - \mathbf{U}_k^H \mathbf{H}_k^{\text{cof}} \mathbf{F}_{\text{cof}} \mathbf{F}_{D,k})^H + \mathbf{U}_k^H \left( \sum_{i \neq k} \mathbf{H}_k^{\text{cof}} \mathbf{F}_{\text{cof}} \mathbf{F}_{D,i} \mathbf{F}_{D,i}^H \mathbf{F}_{\text{cof}}^H (\mathbf{H}_k^{\text{cof}})^H + \sigma_k^2 \mathbf{I} \right) \mathbf{U}_k. \quad (49)$$

This optimization problem can still be solved using the BCD method, where the optimal solution of  $\{\mathbf{W}, \mathbf{U}\}$  can still be obtained from (36) and (37), given that  $\mathbf{H}_k = \mathbf{H}_k^{\text{cof}} \mathbf{F}_{\text{cof}}$ . The key difference lies in the per-antenna optimization of  $\mathbf{F}_{\text{cof}}$  and  $\mathbf{F}_D$ , as outlined in the following subsection.

### A. Per-Antenna Optimization of $\mathbf{F}_{\text{cof}}$ and $\mathbf{F}_D$

Following the per-antenna optimization framework, we now focus on optimize  $\mathbf{f}_{(n)}, \mathbf{c}_{(n)}$  to maximize (48a). Similar to Lemma 1, based on the expression  $\mathbf{H}_k^{\text{cof}} \mathbf{F}_{\text{cof}} \mathbf{F}_{D,i} = \sum_{n=1}^N \mathbf{H}_{(n),k}^{\text{cof}} \mathbf{c}_{(n)} \mathbf{f}_{(n),i}^H$ , we can recast the per-antenna optimization as the following problem:

$$\begin{aligned} \min_{\mathbf{f}_{(n)}, \mathbf{c}_{(n)}} \quad & \|\mathbf{f}_{(n)}\|_2^2 \mathbf{c}_{(n)}^T \mathbf{B}_{nn} \mathbf{c}_{(n)} + 2\text{Re} \left( \mathbf{f}_{(n)}^H (\mathbf{Q}_n - \mathbf{D}_n) \mathbf{c}_{(n)} \right) \\ \text{s.t.} \quad & \|\mathbf{f}_{(n)}\|_2^2 \leq P_n, \\ & \|\mathbf{c}_{(n)}\|_2^2 = 4\pi, \end{aligned} \quad (50a)$$

$$(50b)$$

where  $\mathbf{B}_{nn}$ ,  $\mathbf{Q}_n$ , and  $\mathbf{D}_n$  can be computed via (42)–(44) by repalcing  $\{\mathbf{H}_{(n),k}^{\text{sel}}, \mathbf{b}_{(n)}\}$  with  $\{\mathbf{H}_{(n),k}^{\text{cof}}, \mathbf{c}_{(n)}\}$ . Here,  $\mathbf{H}_{(n),k}^{\text{cof}} \in \mathbb{C}^{M_k \times T}$  is defined as a submatrix of  $\mathbf{H}_k^{\text{cof}}$  such that  $\mathbf{H}_k^{\text{cof}} = [\mathbf{H}_{(1),k}^{\text{cof}}, \dots, \mathbf{H}_{(N),k}^{\text{cof}}] \in \mathbb{C}^{M_k \times NT}$ . Since  $\mathbf{c}_{(n)} \in \mathbb{R}_+^T$  has infinitely many possible configurations, exhaustive enumeration is not applicable. Therefore, we adopt the BCD method again and alternately optimize  $\mathbf{f}_{(n)}$  and  $\mathbf{c}_{(n)}$ .

1) *Optimizing  $\mathbf{f}_{(n)}$  given  $\mathbf{c}_{(n)}$* : Using Proposition 1, the optimal  $\mathbf{f}_{(n)}$  for a fixed  $\mathbf{c}_{(n)}$  is given by:

$$\mathbf{f}_{(n)}^{\text{opt}} = \min \left( \frac{(\mathbf{D}_n - \mathbf{Q}_n) \mathbf{c}_{(n)}}{\mathbf{c}_{(n)}^T \mathbf{B}_{nn} \mathbf{c}_{(n)}}, \frac{\sqrt{P_n} (\mathbf{D}_n - \mathbf{Q}_n) \mathbf{c}_{(n)}}{\|(\mathbf{Q}_n - \mathbf{D}_n) \mathbf{c}_{(n)}\|_2} \right). \quad (51)$$

2) *Optimizing  $\mathbf{c}_{(n)}$  given  $\mathbf{f}_{(n)}$* : However, the optimization of  $\mathbf{c}_{(n)}$  given a fixed  $\mathbf{f}_{(n)}$ , formulated as:

$$\begin{aligned} \min_{\mathbf{c}_{(n)}} \quad & \|\mathbf{f}_{(n)}\|_2^2 \mathbf{c}_{(n)}^T \mathbf{B}_{nn} \mathbf{c}_{(n)} + 2\text{Re} \left\{ \mathbf{f}_{(n)}^H (\mathbf{Q}_n - \mathbf{D}_n) \mathbf{c}_{(n)} \right\} \\ \text{s.t.} \quad & \|\mathbf{c}_{(n)}\|_2^2 = 4\pi, \end{aligned} \quad (52)$$

does not admit a closed-form solution.<sup>1</sup> Before delve into the solution of (52), we reveal an implicit constraint involved.

Recalling (27), we note that there is an implicit constraint on  $\mathbf{c}_{(n)}$  that the synthesized radiation pattern needs to be strictly positive, as demonstrated in Remark 2. However, (52) does not include this constraint, potentially leading to an optimized radiation pattern with non-positive values, which has no physical feasibility. By further examining (27), we observe that the first entry in  $\gamma(\theta, \phi)$  is the 0<sup>th</sup>-order spherical harmonics  $Y_0^0(\theta, \phi)$ , which is a sphere with a constant positive value across all  $(\theta, \phi)$ . Therefore, under the power constraint in (52), we can always assign a sufficiently large coefficient to  $Y_0^0(\theta, \phi)$  to ensure a strictly positive radiation pattern throughout the optimization process. To do so, we fixed the first entry in  $\mathbf{c}_{(n)}$  as  $2\sqrt{\rho\pi}$  and partition

$$\mathbf{c}_{(n)} = \begin{bmatrix} 2\sqrt{\rho\pi} & 2\sqrt{(1-\rho)\pi} \tilde{\mathbf{c}}_{(n)}^T \end{bmatrix}^T \in \mathbb{R}^T, \quad (53)$$

where then  $\tilde{\mathbf{c}}_{(n)} \in \mathbb{R}^{T-1}$  is the variable we optimize with the power constraint converted as  $\|\tilde{\mathbf{c}}_{(n)}\|_2^2 = 1$ . Here,  $\rho \in (0, 1]$  is a factor indicating the strength of the constant component in the synthesized radiation pattern.<sup>2</sup> A smaller value of  $\rho$  stands for a higher degree of freedom afforded to  $\mathbf{c}_{(n)}$ .

<sup>1</sup>Although the global optimum of (52) does not have a closed-form expression, [35] shows that closed-form solutions exist for two local optima.

<sup>2</sup>As an empirical guideline, maintaining  $\rho > 0.7$  generally ensures that the synthesized radiation pattern remains positive over the sphere.

By substituting (53) into (52) and omit constant terms, one can further recast (52) as:

$$\min_{\tilde{\mathbf{c}}_{(n)}} \quad \tilde{\mathbf{c}}_{(n)}^T \tilde{\mathbf{B}}_{nn} \tilde{\mathbf{c}}_{(n)} + (\mathbf{v}_1 + \mathbf{v}_2)^T \tilde{\mathbf{c}}_{(n)} \quad (54a)$$

$$\text{s.t.} \quad \|\tilde{\mathbf{c}}_{(n)}\|_2^2 = 1, \quad (54b)$$

where  $\tilde{\mathbf{B}}_{nn} = 4\pi(1 - \rho)\|\mathbf{f}_{(n)}\|_2^2[\mathbf{B}_{nn}]_{2:T,2:T}$ ,  $\mathbf{v}_1 = 4\sqrt{(1-\rho)\pi}\text{Re}\{\mathbf{f}_{(n)}^H[\mathbf{Q}_n - \mathbf{D}_n]_{:,2:T}\}$ , and  $\mathbf{v}_2 = 8\pi\sqrt{\rho(1-\rho)}\|\mathbf{f}_{(n)}\|_2^2\text{Re}\{[\mathbf{B}_{nn}]_{2:T,1}\}$ . We employ the Riemannian manifold optimization technique to solve (54). The detailed steps are presented in the next subsection.

### B. Solving (54) Using Riemannian Manifold Optimization

Riemannian manifold optimization is a method for solving constrained problems by exploiting the geometry of the constraint set. Instead of operating in the full Euclidean space, it performs optimization directly on smooth manifolds where the constraints naturally define the search space [39]–[41]. In our case, the constraint (54b) corresponds to a unit 2-norm sphere. We define the unit 2-norm manifold as

$$\mathbb{M} \triangleq \{\mathbf{x} \in \mathbb{R}^{T-1} \mid \|\mathbf{x}\|_2^2 = 1\}. \quad (55)$$

Next, we can rewrite (54) in a unconstrained form as

$$\min_{\tilde{\mathbf{c}}_{(n)} \in \mathbb{M}} \quad \tilde{\mathbf{c}}_{(n)}^T \tilde{\mathbf{B}}_{nn} \tilde{\mathbf{c}}_{(n)} + (\mathbf{v}_1 + \mathbf{v}_2)^T \tilde{\mathbf{c}}_{(n)}. \quad (56)$$

Similar to the gradient-based algorithms in Euclidean space, optimization over a Riemannian manifold is implemented by using the *Riemannian gradient* [39], [42], [43]. We denote the objective function in (56) as  $g(\tilde{\mathbf{c}}_{(n)})$ . At iteration  $j$ , given the previous candidate variable  $\tilde{\mathbf{c}}_{(n)}^{[j-1]}$ , we first compute the Euclidean gradient as

$$\nabla_{\tilde{\mathbf{c}}_{(n)}^{[j-1]}} g = (\tilde{\mathbf{B}}_{nn} + \tilde{\mathbf{B}}_{nn}^T) \tilde{\mathbf{c}}_{(n)}^{[j-1]} + \mathbf{v}_1 + \mathbf{v}_2. \quad (57)$$

Next, the Riemannian gradient is obtained by projecting the calculated Euclidean gradient onto the tangent space at point  $\tilde{\mathbf{c}}_{(n)}^{[j-1]}$  of the manifold  $\mathbb{M}$ . Mathematically, the tangent space at a point  $\tilde{\mathbf{c}}_{(n)} \in \mathbb{M}$  is defined as

$$\mathcal{T}_{\tilde{\mathbf{c}}_{(n)}} \mathbb{M} \triangleq \{\mathbf{x} \in \mathbb{R}^{T-1} \mid \mathbf{x}^T \tilde{\mathbf{c}}_{(n)} = 0\}, \quad (58)$$

and the projection operation is given by

$$\text{Proj}_{\tilde{\mathbf{c}}_{(n)}}(\nabla_{\tilde{\mathbf{c}}_{(n)}} g) = \nabla_{\tilde{\mathbf{c}}_{(n)}} g - (\tilde{\mathbf{c}}_{(n)}^T \nabla_{\tilde{\mathbf{c}}_{(n)}} g) \tilde{\mathbf{c}}_{(n)}. \quad (59)$$

We then update the optimization variable in the Riemannian gradient direction and finally retract it from the tangent space  $\mathcal{T}_{\tilde{\mathbf{c}}_{(n)}^{[j-1]}} \mathbb{M}$  onto the manifold  $\mathbb{M}$ , thus obtaining new candidate variable  $\tilde{\mathbf{c}}_{(n)}^{[j]}$ . These update and retraction operations in unit 2-norm sphere can be implemented as

$$\tilde{\mathbf{c}}_{(n)}^{[j]} = \frac{\tilde{\mathbf{c}}_{(n)}^{[j-1]} - \varepsilon \text{Proj}_{\tilde{\mathbf{c}}_{(n)}^{[j-1]}}(\nabla_{\tilde{\mathbf{c}}_{(n)}^{[j-1]}} g)}{\left\| \tilde{\mathbf{c}}_{(n)}^{[j-1]} - \varepsilon \text{Proj}_{\tilde{\mathbf{c}}_{(n)}^{[j-1]}}(\nabla_{\tilde{\mathbf{c}}_{(n)}^{[j-1]}} g) \right\|_2}, \quad (60)$$

where  $\varepsilon \in \mathbb{R}_+$  is the step size. This update procedure ensures that the iterations always proceed within the manifold  $\mathbb{M}$ .

---

**Algorithm 2** Tyi-Hybrid Precoding Based on Model II
 

---

- 1: **Input:**  $\mathbf{H}_k^{\text{cof}}, \sigma_k^2, \forall k$ .     **Output:**  $\mathbf{F}_{\text{cof}}^{\text{opt}}, \mathbf{F}_{\text{RF}}^{\text{opt}}, \mathbf{F}_{\text{BB}}^{\text{opt}}$ .
  - 2: Initialize  $\mathbf{F}_{\text{cof}}, \mathbf{F}_{\text{RF}}, \mathbf{F}_{\text{BB}}, \mathbf{F}_{\text{D}} = \mathbf{F}_{\text{RF}} \mathbf{F}_{\text{BB}}, \mathbf{W}_k = \mathbf{I}$ , and the maximum iteration number  $I_{\text{max}}$ .
  - 3: **for**  $\text{Iter} = 1, 2, \dots, I_{\text{max}}$  **do**
  - 4:   Compute  $\mathbf{H}_k = \mathbf{H}_k^{\text{cof}} \mathbf{F}_{\text{cof}}, \forall k$ .
  - 5:   Update  $\mathbf{U}_k = \mathbf{U}_k^{\text{opt}}, \forall k$ , according to (36).
  - 6:   Update  $\mathbf{W}_k = \mathbf{W}_k^{\text{opt}}, \forall k$ , according to (37).
  - 7:   **for**  $n = 1, 2, \dots, N$  **do**
  - 8:     Compute  $\{\mathbf{B}_{nn}, \mathbf{Q}_n, \mathbf{D}_n\}$  via (42)–(44) by replacing  $\{\mathbf{H}_{(n),k}^{\text{sel}}, \mathbf{b}_{(n)}\}$  with  $\{\mathbf{H}_{(n),k}^{\text{cof}}, \mathbf{c}_{(n)}\}$ .
  - 9:     Compute the optimal  $\mathbf{f}_{(n)}^{\text{opt}}$  given  $\mathbf{c}_{(n)}$  via (51).
  - 10:    Obtain  $\mathbf{c}_{(n)}^{\text{opt}}$  given  $\mathbf{f}_{(n)}^{\text{opt}}$  using the approach described in Section V-B.
  - 11:   **end for**
  - 12:   Recover  $\mathbf{F}_{\text{cof}}^{\text{opt}}$  and  $\mathbf{F}_{\text{D}}^{\text{opt}}$  based on  $\{\mathbf{f}_{(n)}^{\text{opt}}, \mathbf{c}_{(n)}^{\text{opt}}\}_{n=1}^N$  using (29) and (38), respectively.
  - 13: **end for**
  - 14: Decompose  $\mathbf{F}_{\text{D}}^{\text{opt}}$  back into  $\mathbf{F}_{\text{RF}}^{\text{opt}}$  and  $\mathbf{F}_{\text{BB}}^{\text{opt}}$  using the method described in Section IV-C.
- 

### C. Algorithm Summary and Complexity Analysis

As a result, the proposed tri-hybrid precoding algorithm based on Model II is summarized in Algorithm 2.

The computational complexity of Algorithm 1 is analyzed as follows. Under the same assumption that  $N \gg \sum_{k=1}^K M_k > D > K$ , we focus on the complexity with respect to the number of BS antennas  $N$  and the spherical harmonics truncation length  $T$ . The complexity of lines 4–6 is dominated by line 4, which has a complexity of  $\mathcal{O}(N^2T)$ . Over the loop in line 7, the operation in line 8 incurs a total complexity of  $\mathcal{O}(NT^2)$ , the updates in lines 9 contribute a total complexity of  $\mathcal{O}(NT^2)$ , and the Riemannian manifold optimization method in line 10 incurs a total complexity of  $\mathcal{O}(NT^2)$ . Additionally, the decomposition method in line 17 has a complexity of  $\mathcal{O}(N_{\text{RF}}^2N)$  when Algorithm 1 in [26] is adopted. Therefore, the overall complexity of Algorithm 2 can be summarized as  $\mathcal{O}(I_{\text{max}}(N^2T + NT^2 + N_{\text{RF}}^2N))$ .

## VI. SIMULATION RESULTS

This section presents the simulation results to show the performance of the considered tri-hybrid architecture and the proposed precoding algorithms.

### A. Simulation Setup

To assess performance of our developed models and precoding algorithms in realistic scenarios, we generate the multi-user channels using ray-tracing simulation, as illustrated in Fig. 4. The BS is equipped with a  $10 \times 10$  half-wavelength spaced antenna array. Three UEs are deployed in the scene, each configured with a  $2 \times 2$  half-wavelength spaced antenna array. The ray-tracing simulations are carried out using Sionna RT in an example environment based on the area around the Frauenkirche in Munich, Germany [44]. To accurately capture spatial characteristics, we perform per-antenna ray tracing,

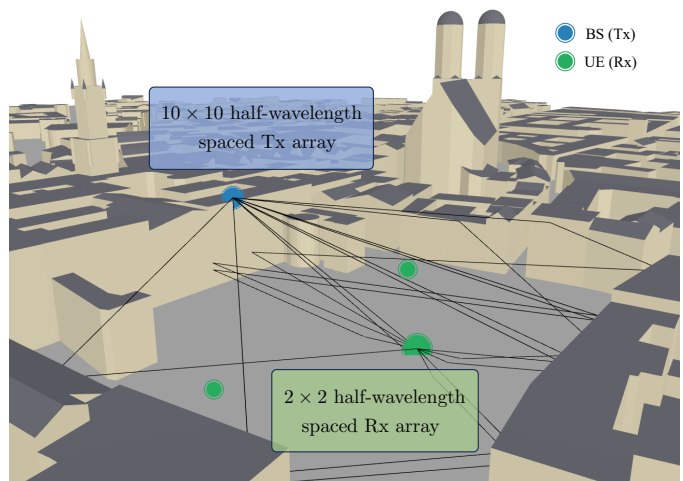


Fig. 4. Ray-tracing results generated using Sionna RT in an example scene set in Munich, Germany. The scenario consists of a BS with a  $10 \times 10$  antenna array and three UEs, each equipped with a  $2 \times 2$  antenna array. Both the BS and UEs are configured with half-wavelength spacing. For clarity, ray-tracing results are depicted for one representative UE only.

allowing the channel parameters for each antenna element to be independently simulated. The simulation includes both line-of-sight (LoS) paths and non-line-of-sight (NLoS) paths with up to triple-bounce reflections, as shown in Fig. 4. From these simulations, we extract the complex channel gains, propagation delays, AoDs, and AoAs for each per-antenna link. These parameters are then used to construct the wireless channel according to (11), and to compute the effective channels as defined in (23) and (31).

Unless otherwise specified, the system parameters are set as follows. The carrier frequency is set to 30 GHz in the mmWave band. Each UE is allocated two data streams, i.e.,  $D_k = 2, \forall k$ . The number of RF chains at the BS is set to  $N_{\text{RF}} = D + 3 = (\sum_{k=1}^K D_k) + 3 = 9$ . The per-antenna power budget at the BS is  $P_n = 0$  dBm,  $\forall n$ , and the noise power at each UE is  $\sigma_k^2 = -90$  dBm,  $\forall k$ . Equal weights are assigned to the three users, i.e.,  $\beta_1 = \beta_2 = \beta_3 = 1/3$ . For Model I, we use the 64 available radiation patterns from the real pattern-reconfigurable antenna prototype in [22]. For Model II, antenna patterns are arbitrarily optimized based on spherical harmonics decomposition, with the 0<sup>th</sup>-order component fixed at  $\rho = 0.7$  and a truncation length of  $T = 49$ . Moreover, when evaluating the conventional hybrid MIMO benchmark, the reconfigurability of the antenna radiation patterns is disabled, and all antennas are assigned a fixed radiation pattern. This fixed pattern corresponds to State 2 in Fig. 2.

### B. Performance Evaluation

1) *Antenna Radiation Pattern Visualization:* In Fig. 5-(a), we visualize the multipath departure directions from a selected BS antenna to the three UEs. The length of each arrow is inversely proportional to the path loss, i.e., proportional to the signal strength. Figures 5-(b) and 5-(c) plot the optimized radiation patterns at this antenna based on Model I and Model II, respectively. In Model I, the proposed algorithm successfully selects the optimal candidate pattern that directs power toward

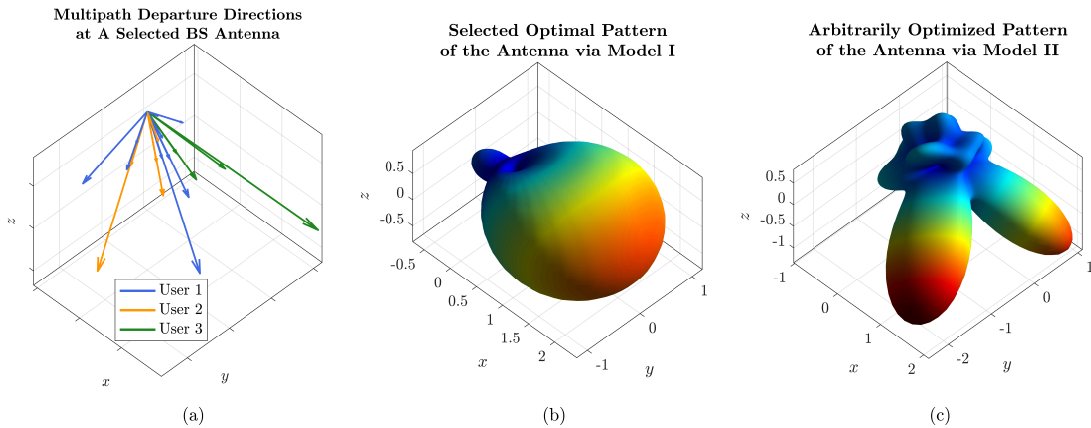


Fig. 5. Visualization of the multipath geometry and the optimized antenna radiation patterns for a selected antenna element at the BS, under the two models. (a) Multipath departure directions from the selected antenna to the three UEs, where the length of each arrow is inversely proportional to the path loss, i.e., proportional to the signal strength. (b) Optimized radiation pattern based on Model I. (c) Optimized radiation pattern based on Model II.

the dominant multipath directions. However, this approach is limited by the constrained degrees of freedom inherent in real antenna designs. In contrast, the arbitrary optimization results under Model II yield a more tailored radiation pattern that more precisely steers power toward the strongest multipath directions while also accounts for weaker paths. From an intuitive perspective, the proposed algorithms based on both models return reasonable and meaningful results.

2) *Array Beampattern Visualization*: Subsequently, we illustrate in Fig. 6 the array beampatterns optimized under different antenna configurations. Following the formulation in [45, Eq. (9)–(11)], the array beampattern for the  $k^{\text{th}}$  UE is computed as

$$E_k(\theta, \phi) = \|\mathbf{r}^T(\theta, \phi)\mathbf{F}_{\text{RF}}\mathbf{F}_{\text{BB},k}\|_2, \quad (61)$$

where  $\mathbf{r}(\theta, \phi) \in \mathbb{C}^N$  denotes the array manifold vector. Specifically, the  $n^{\text{th}}$  entry of  $\mathbf{r}(\theta, \phi)$  is given by  $r_n(\theta, \phi) = G_{(n)}^{\text{BS}}(\theta, \phi)e^{j\frac{2\pi}{\lambda}\mathbf{p}_n^T\mathbf{u}(\theta, \phi)}$ , where  $\mathbf{p}_n$  denotes the position of the  $n^{\text{th}}$  antenna in the BS’s body coordinate system, and  $\mathbf{u}(\theta, \phi)$  is a unit directional vector defined as  $\mathbf{u}(\theta, \phi) = [\sin\theta\cos\phi, \sin\theta\sin\phi, \cos\theta]^T$ . In the three subfigures of Fig. 6, the BS antenna radiation patterns  $G_{(n)}^{\text{BS}}(\theta, \phi)$  (for all  $n$ ) are configured as fixed, optimized using Model I, and optimized using Model II, respectively. To offer a intuitive two-dimensional (2D) illustration, Fig. 6 plots the envelope of the beampattern over the azimuth angle  $\phi$ , which is obtained as  $\tilde{E}_k(\phi) = \max_{\theta} E_k(\theta, \phi)$ .

While the multi-user precoding objective cannot be directly visualized due to inter-user interference, some intuitive insights can still be gleaned from the figure. In general, the additional degrees of freedom provided by reconfigurable antenna radiation patterns allow the array beampattern to allocate power more effectively toward the dominant multipath directions. For instance, in the fixed-antenna case, the system fails to leverage the LoS paths to User 2 and User 3, resulting in their normalized gains being lower than  $-10$  dB. In contrast, under the reconfigurable cases, particularly Model II, these two LoS paths receive significantly more power, leading to a substantially higher weighted sum-rate for the system. In addition, the limitations of the proposed precoding algorithm under

the WMMSE framework are also evident here. For example, in all three cases, the beampatterns for User 1 and User 3 fail to direct their main lobes toward reasonable directions. This suboptimality arises from the BCD routine used in our optimization, which cannot guarantee global optimality. Thus, there still remains potential for further improvement from the algorithmic perspective.

3) *Weighted Sum-Rate versus Transmit Power*: Next, we evaluate the performance gain offered by the proposed tri-hybrid MIMO architecture in comparison to the conventional hybrid MIMO design. Figure 7 demonstrates the weighted sum-rate as a function of the BS per-antenna power budget across different system architectures. Alongside the tri-hybrid architecture optimized under both Model I and Model II, we also include the conventional hybrid architecture with fixed antennas, optimized using two benchmark methods: the WMMSE precoding algorithm [28] and the zero-forcing (ZF) algorithm [46], all under the same per-antenna power constraint. Note that under Model I, besides the set of 64 real antenna patterns in [22] (denoted as “Model I, hardware”), we further add a benchmark set of 64 fictitious antenna patterns (denoted as “Model I, fictitious”). These fictitious patterns are set as Gaussian beams steered toward 64 directions uniformly distributed within  $\theta \in [90^\circ, 180^\circ]$  and  $\phi \in [-90^\circ, 90^\circ]$ , each with a 3 dB beamwidth of  $85^\circ$ . Additionally, we present both the fully digital solutions and those obtained by decomposing the digital precoder back into digital and hybrid components. The results indicate that the decomposition method proposed in Section IV-C effectively preserves the overall weighted sum-rate, with only minor performance degradation for the tri-hybrid solutions and the WMMSE-based hybrid solution. Regarding the comparison between system architectures, the tri-hybrid architecture consistently outperforms the conventional hybrid design; however, the Model I-based solution based on real hardware provides only a minor gain of up to 0.9 bps/Hz, while the Model II-based solution delivers a much more substantial improvement of up to 5.8 bps/Hz. This highlights the limited benefit of the existing pattern-reconfigurable antenna hardware in [22] due to its restricted flexibility. Nonetheless, the significant performance gain observed under Model II

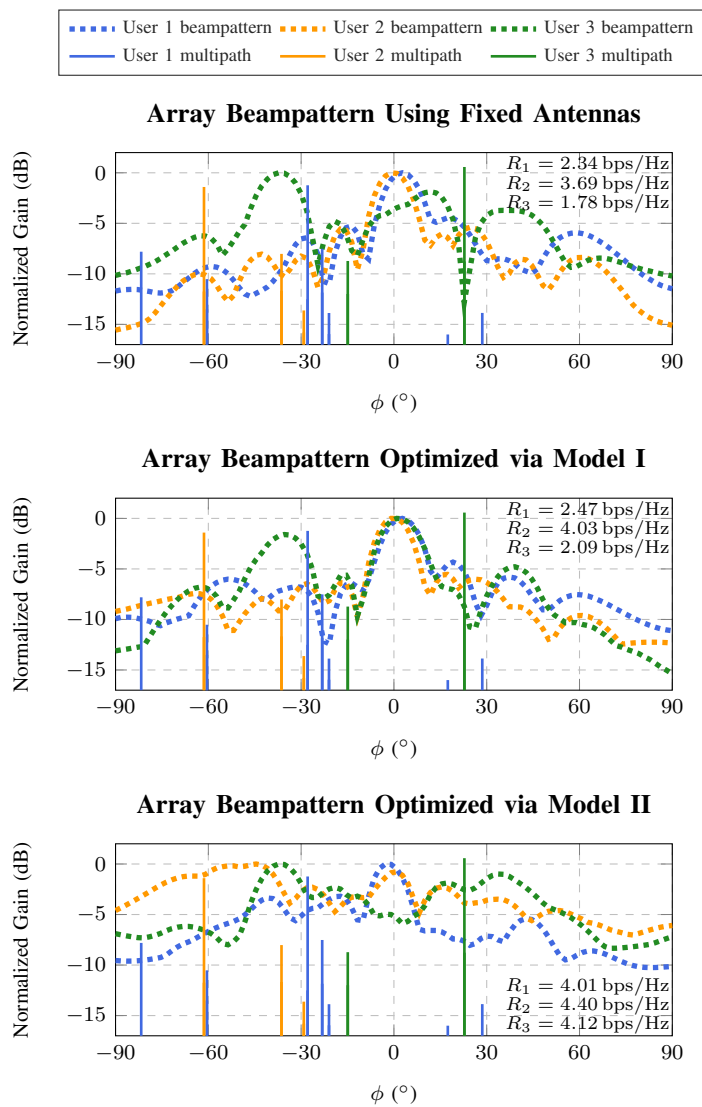


Fig. 6. Visualization of the array beampattern under different antenna setups. The antenna gains are normalized with respect to their maximum value.

emphasizes the strong potential of the tri-hybrid architecture with future advancements in reconfigurable antenna design and fabrication. Moreover, the performance of Model I with fictitious patterns suggests that arbitrary pattern generation may not be strictly necessary. Substantial gains can also be achieved by designing a more effective set of limited patterns. A promising strategy for this design is to use Model II as a guiding reference for optimizing the selection/design of practical pattern sets.

4) *Hardware Efficiency Evaluation:* Apart from the performance gain, this technology holds strong potential for reducing reliance on costly system components. To validate this, Fig. 8 and Fig. 9 illustrate the weighted sum-rate as a function of the number of BS RF chains  $N_{\text{RF}}$  and the number of BS antennas  $N$ , respectively. The results in both figures show that system performance generally improves with an increasing number of RF chains or antennas. In these two figures, we also evaluate the performance of Model II under various values of the 0<sup>th</sup>-order harmonic strength  $\rho$ , as defined in (53). A lower value

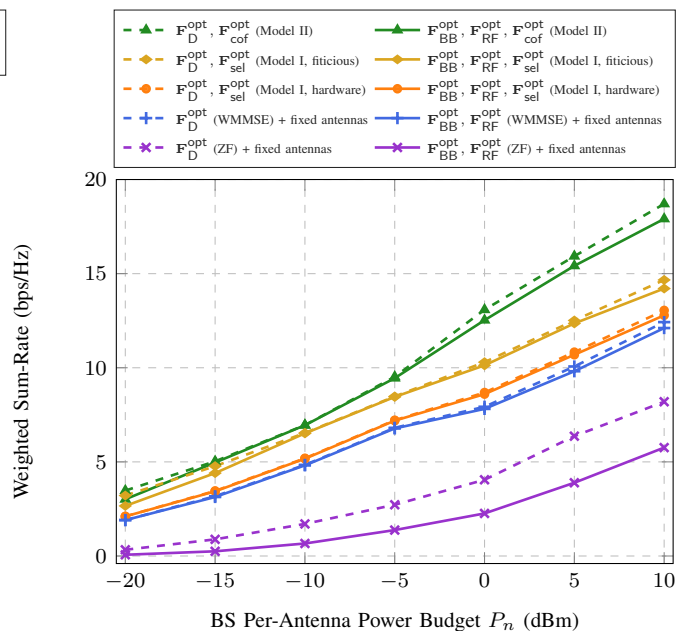


Fig. 7. Evaluation of weighted sum-rate versus BS per-antenna power budget.

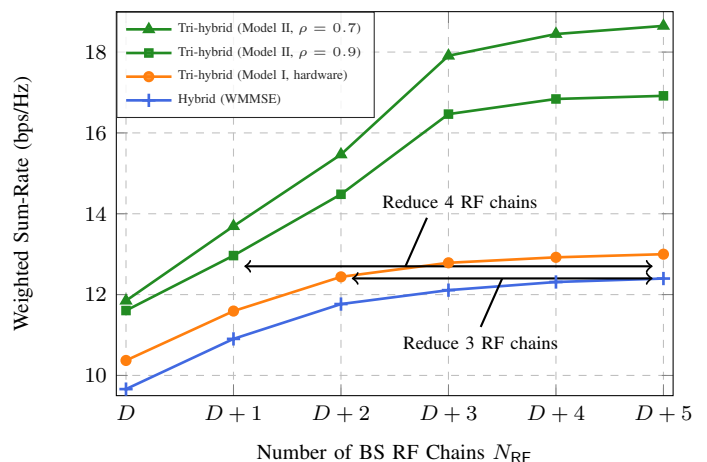


Fig. 8. Evaluation of weighted sum-rate versus number of BS RF chains, where  $D = 6$  is the total number of data streams required by all users.

of  $\rho$  corresponds to greater flexibility in spherical harmonics-based radiation pattern synthesis. It is evident that increased flexibility in radiation pattern synthesis leads to more significant enhancements in system sum-rate. Moreover, as shown in Fig. 8 and Fig. 9, the Model I-based tri-hybrid solution adopting the real hardware patterns can achieve the same level of system sum-rate while reducing three RF chains or approximately 10% of the antennas. In contrast, the Model II-based tri-hybrid solution with  $\rho = 0.9$  can reduce four RF chains or approximately 57% of the antennas without compromising performance. Besides, we also observe that when  $N_{\text{RF}}$  and  $N$  is small, the hardware cost reduction provided by the tri-hybrid architecture is less pronounced. However, in these regions, since the hardware cost is already low, performance improvement becomes the primary concern. As shown in the both figures, the proposed architecture still offers substantial performance gains in regions with low  $N_{\text{RF}}$  and  $N$ . These

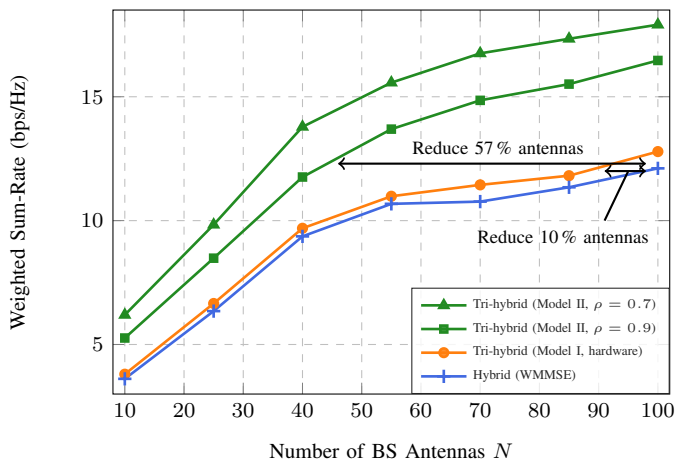


Fig. 9. Evaluation of weighted sum-rate versus number of BS antennas.

findings demonstrate the potential of the pattern-reconfigurable antenna-based tri-hybrid architecture in enabling low-cost and energy-efficient MIMO communications.

## VII. CONCLUSION

This paper investigates a tri-hybrid MIMO architecture that integrates digital, analog, and antenna-domain precoding via pattern-reconfigurable antennas for multi-user communication. The primary contribution lies in the development of two channel models to capture varying levels of radiation pattern flexibility and develop the WMMSE-based precoding algorithms with practical power constraints and quadratic complexity. The developed two models evaluate the system performance under two scenarios: (i) a practical setting constrained by existing pattern-reconfigurable antenna hardware, and (ii) an idealized case where arbitrary radiation patterns can be synthesized. The results allow us to answer the two questions posed in Section I. For Q1, under current hardware limitations in [22], the achievable performance gain is modest, yielding approximately 0.9 bps/Hz in our simulation environment. However, with more advanced hardware supporting greater pattern flexibility, the performance gain can be substantial, exceeding 5.8 bps/Hz. For Q2, the proposed tri-hybrid architecture is shown to significantly reduce the number of RF chains and antennas without compromising system performance. Moreover, the higher the degree of pattern reconfigurability, the greater the potential for hardware cost savings.

Nonetheless, a key limitation of this work lies in the reliance of the proposed algorithm on an alternating optimization framework, which does not guarantee global optimality. Additionally, there remains considerable room for improving the algorithm's computational efficiency. Future research directions include the development of more efficient optimization techniques, the design of more flexible pattern-reconfigurable antennas, the incorporation of more realistic effects (such as mutual coupling and polarization), and initial experimental validation of the tri-hybrid MIMO system.

## APPENDIX

Based on Lemma 1, the optimization of  $\mathbf{f}_{(n)}$  in (39) given a fixed  $\mathbf{b}_{(n)}$  can be rewritten as

$$\min_{\mathbf{f}_{(n)}} a \|\mathbf{f}_{(n)}\|_2^2 + 2\text{Re}(\mathbf{f}_{(n)}^H \mathbf{d}) \quad (\text{A.1a})$$

$$\text{s.t.} \quad \|\mathbf{f}_{(n)}\|_2^2 \leq P_n, \quad (\text{A.1b})$$

where  $a = \mathbf{b}_{(n)}^T \mathbf{B}_{nn} \mathbf{b}_{(n)} > 0$  and  $\mathbf{d} = (\mathbf{Q}_n - \mathbf{D}_n) \mathbf{b}_{(n)}$ . It can be inferred that the optimal solution  $\mathbf{f}_{(n)}^{\text{opt}}$  must be parallel and opposite to  $\mathbf{d}$ , i.e.,

$$\mathbf{f}_{(n)}^{\text{opt}} = -x \mathbf{d}, \quad x \in \mathbb{R}_+. \quad (\text{A.2})$$

This can be proven by contradiction: suppose there exists an optimal solution  $\mathbf{f}_{(n)}^{\text{opt}}$  to (A.1) that does not conform to (A.2). Then, we have  $(\mathbf{f}_{(n)}^{\text{opt}})^H \mathbf{d} > -\|\mathbf{f}_{(n)}^{\text{opt}}\|_2 \|\mathbf{d}\|_2$ . In this case, we can always construct a new vector  $\tilde{\mathbf{f}}_{(n)}^{\text{opt}} = -\frac{\|\mathbf{f}_{(n)}^{\text{opt}}\|_2}{\|\mathbf{d}\|_2} \mathbf{d}$ , which yields a lower objective value in (A.1a) than  $\mathbf{f}_{(n)}^{\text{opt}}$ . This contradiction implies that  $\mathbf{f}_{(n)}^{\text{opt}}$  cannot be optimal, and hence (A.2) must hold.

Substituting (A.2) into (A.1a), the optimization problem becomes  $\min_x a x^2 - 2x$ , s.t.  $x \leq \sqrt{P_n} / \|\mathbf{d}\|_2$ , whose optimal solution is given by  $x^{\text{opt}} = \min\left(\frac{1}{a}, \frac{\sqrt{P_n}}{\|\mathbf{d}\|_2}\right)$ . Combining this with (A.2) gives the expression for  $\mathbf{f}_{(n)}^{\text{opt}}$  in (45).

## REFERENCES

- [1] A. Paulraj, D. Gore, R. Nabar, and H. Bolcskei, "An overview of MIMO communications—a key to gigabit wireless," *Proceedings of the IEEE*, vol. 92, no. 2, pp. 198–218, 2004.
- [2] Q. Li, G. Li, W. Lee, M.-i. Lee, D. Mazzaresse, B. Clerckx, and Z. Li, "MIMO techniques in WiMAX and LTE: a feature overview," *IEEE Communications Magazine*, vol. 48, no. 5, pp. 86–92, 2010.
- [3] J. Kim and I. Lee, "802.11 WLAN: history and new enabling MIMO techniques for next generation standards," *IEEE Communications Magazine*, vol. 53, no. 3, pp. 134–140, 2015.
- [4] S. Parkvall, E. Dahlman, A. Furuskar, and M. Frenne, "NR: The new 5G radio access technology," *IEEE Communications Standards Magazine*, vol. 1, no. 4, pp. 24–30, 2017.
- [5] A. Alkhateeb, J. Mo, N. Gonzalez-Prelcic, and R. W. Heath, "MIMO precoding and combining solutions for millimeter-wave systems," *IEEE Communications Magazine*, vol. 52, no. 12, pp. 122–131, 2014.
- [6] F. Sahrabi and W. Yu, "Hybrid digital and analog beamforming design for large-scale antenna arrays," *IEEE Journal of Selected Topics in Signal Processing*, vol. 10, no. 3, pp. 501–513, 2016.
- [7] X. Gao, L. Dai, S. Han, C.-L. I, and R. W. Heath, "Energy-efficient hybrid analog and digital precoding for mmWave MIMO systems with large antenna arrays," *IEEE Journal on Selected Areas in Communications*, vol. 34, no. 4, pp. 998–1009, 2016.
- [8] T. L. Marzetta, "Massive MIMO: An introduction," *Bell Labs Technical Journal*, vol. 20, pp. 11–22, 2015.
- [9] E. D. Carvalho, A. Ali, A. Amiri, M. Angelichinoski, and R. W. Heath, "Non-stationarities in extra-large-scale massive MIMO," *IEEE Wireless Communications*, vol. 27, no. 4, pp. 74–80, 2020.
- [10] J. G. Andrews, T. E. Humphreys, and T. Ji, "6G takes shape," *IEEE BITS the Information Theory Magazine*, vol. 4, no. 1, pp. 2–24, 2024.
- [11] J. D. Boerman and J. T. Bernhard, "Performance study of pattern reconfigurable antennas in MIMO communication systems," *IEEE Transactions on Antennas and Propagation*, vol. 56, no. 1, pp. 231–236, 2008.
- [12] R. Deng, Y. Zhang, H. Zhang, B. Di, H. Zhang, H. V. Poor, and L. Song, "Reconfigurable holographic surfaces for ultra-massive MIMO in 6G: Practical design, optimization and implementation," *IEEE Journal on Selected Areas in Communications*, vol. 41, no. 8, pp. 2367–2379, 2023.
- [13] R. J. Williams, P. Ramirez-Espinosa, J. Yuan, and E. de Carvalho, "Electromagnetic based communication model for dynamic metasurface antennas," *IEEE Transactions on Wireless Communications*, vol. 21, no. 10, pp. 8616–8630, 2022.

- [14] K.-K. Wong, A. Shojaeifard, K.-F. Tong, and Y. Zhang, "Fluid antenna systems," *IEEE Transactions on Wireless Communications*, vol. 20, no. 3, pp. 1950–1962, 2021.
- [15] J. Costantine, Y. Tawk, S. E. Barbin, and C. G. Christodoulou, "Reconfigurable antennas: Design and applications," *Proceedings of the IEEE*, vol. 103, no. 3, pp. 424–437, 2015.
- [16] R. L. Haupt and M. Lanagan, "Reconfigurable antennas," *IEEE Antennas and Propagation Magazine*, vol. 55, no. 1, pp. 49–61, 2013.
- [17] K. Ying, Z. Gao, Y. Su, T. Qin, M. Matthaiou, and R. Schober, "Reconfigurable massive MIMO: Precoding design and channel estimation in the electromagnetic domain," *IEEE Transactions on Communications*, 2024, early access.
- [18] M. R. Castellanos and R. W. Heath, "Linear polarization optimization for wideband MIMO systems with reconfigurable arrays," *IEEE Transactions on Wireless Communications*, vol. 23, no. 3, pp. 2282–2295, 2024.
- [19] M. R. Castellanos, S. Yang, C.-B. Chae, and R. W. Heath Jr, "Embracing reconfigurable antennas in the tri-hybrid MIMO architecture for 6G," *arXiv preprint arXiv:2501.16610*, 2025.
- [20] M. R. Castellanos, J. Carlson, and R. W. Heath, "Energy-efficient tri-hybrid precoding with dynamic metasurface antennas," in *2023 57th Asilomar Conference on Signals, Systems, and Computers*, 2023, pp. 1625–1630.
- [21] P. Zheng, M. J. Hossain, and A. Chaaban, "Enhanced beam pattern synthesis using electromagnetically reconfigurable antennas," 2025. [Online]. Available: <https://arxiv.org/abs/2503.03856>
- [22] R. Wang, P. Zheng, V. V. Kotte, S. Rauf, Y. Yang, M. M. U. Rahman, T. Y. Al-Naffouri, and A. Shamim, "Electromagnetically reconfigurable fluid antenna system for wireless communications: Design, modeling, algorithm, fabrication, and experiment," 2025. [Online]. Available: <https://arxiv.org/abs/2502.19643>
- [23] M. Liu, M. Li, R. Liu, and Q. Liu, "Tri-timescale beamforming design for tri-hybrid architectures with reconfigurable antennas," *arXiv preprint arXiv:2503.03620*, 2025.
- [24] A. Alkhateeb, G. Leus, and R. W. Heath, "Limited feedback hybrid precoding for multi-user millimeter wave systems," *IEEE Transactions on Wireless Communications*, vol. 14, no. 11, pp. 6481–6494, 2015.
- [25] O. E. Ayach, S. Rajagopal, S. Abu-Surra, Z. Pi, and R. W. Heath, "Spatially sparse precoding in millimeter wave MIMO systems," *IEEE Transactions on Wireless Communications*, vol. 13, no. 3, pp. 1499–1513, 2014.
- [26] H. Huang, M. F. Keskin, H. Wymeersch, X. Cai, L. Wu, J. Thunberg, and F. Tufvesson, "Hybrid precoder design for angle-of-departure estimation with limited-resolution phase shifters," *IEEE Transactions on Communications*, 2024, early access.
- [27] W. Yu and T. Lan, "Transmitter optimization for the multi-antenna downlink with per-antenna power constraints," *IEEE Transactions on Signal Processing*, vol. 55, no. 6, pp. 2646–2660, 2007.
- [28] X. Zhao, S. Lu, Q. Shi, and Z.-Q. Luo, "Rethinking WMMSE: Can its complexity scale linearly with the number of BS antennas?" *IEEE Transactions on Signal Processing*, vol. 71, pp. 433–446, 2023.
- [29] C. A. Balanis, *Antenna theory: analysis and design*. John Wiley & sons, 2016.
- [30] "IEEE standard for definitions of terms for antennas," *IEEE Std 145-2013 (Revision of IEEE Std 145-1993)*, pp. 1–50, 2014.
- [31] S. Tarboush, H. Sameddeen, H. Chen, M. H. Loukil, H. Jemaa, M.-S. Alouini, and T. Y. Al-Naffouri, "TeraMIMO: A channel simulator for wideband ultra-massive MIMO terahertz communications," *IEEE Transactions on Vehicular Technology*, vol. 70, no. 12, pp. 12 325–12 341, 2021.
- [32] P. N. Alevizos, X. Fu, N. D. Sidiropoulos, Y. Yang, and A. Bletsas, "Limited feedback channel estimation in massive MIMO with non-uniform directional dictionaries," *IEEE Transactions on Signal Processing*, vol. 66, no. 19, pp. 5127–5141, 2018.
- [33] P. Zheng, T. Ballal, H. Chen, H. Wymeersch, and T. Y. Al-Naffouri, "Coverage analysis of joint localization and communication in THz systems with 3D arrays," *IEEE Transactions on Wireless Communications*, vol. 23, no. 5, pp. 5232–5247, 2024.
- [34] Z. Han, Y. Zhang, S. Shen, Y. Li, C.-Y. Chiu, and R. Murch, "Characteristic mode analysis of ESPAR for single-RF MIMO systems," *IEEE Transactions on Wireless Communications*, vol. 20, no. 4, pp. 2353–2367, 2021.
- [35] P. Zheng, Y. Zhang, T. Y. Al-Naffouri, M. J. Hossain, and A. Chaaban, "Tri-hybrid multi-user precoding based on electromagnetically reconfigurable antennas," *arXiv preprint arXiv:2505.02254*, 2025.
- [36] Q. Shi, M. Razaviyayn, Z.-Q. Luo, and C. He, "An iteratively weighted MMSE approach to distributed sum-utility maximization for a MIMO interfering broadcast channel," *IEEE Transactions on Signal Processing*, vol. 59, no. 9, pp. 4331–4340, 2011.
- [37] D. P. Bertsekas, "Nonlinear programming," *Journal of the Operational Research Society*, vol. 48, no. 3, pp. 334–334, 1997.
- [38] X. Yu, J.-C. Shen, J. Zhang, and K. B. Letaief, "Alternating minimization algorithms for hybrid precoding in millimeter wave MIMO systems," *IEEE Journal of Selected Topics in Signal Processing*, vol. 10, no. 3, pp. 485–500, 2016.
- [39] N. Boumal, *An introduction to optimization on smooth manifolds*. Cambridge University Press, 2023.
- [40] A. Douik, X. Liu, T. Ballal, T. Y. Al-Naffouri, and B. Hassibi, "Precise 3-D GNSS attitude determination based on Riemannian manifold optimization algorithms," *IEEE Transactions on Signal Processing*, vol. 68, pp. 284–299, 2020.
- [41] P. Zheng, X. Liu, and T. Y. Al-Naffouri, "LEO- and RIS-empowered user tracking: A Riemannian manifold approach," *IEEE Journal on Selected Areas in Communications*, vol. 42, no. 12, pp. 3445–3461, 2024.
- [42] P.-A. Absil, R. Mahony, and R. Sepulchre, "Optimization algorithms on matrix manifolds," in *Optimization Algorithms on Matrix Manifolds*. Princeton University Press, 2009.
- [43] N. Boumal, B. Mishra, P.-A. Absil, and R. Sepulchre, "Manopt, a Matlab toolbox for optimization on manifolds," *Journal of Machine Learning Research*, vol. 15, no. 42, pp. 1455–1459, 2014. [Online]. Available: <https://www.manopt.org>
- [44] J. Hoydis, S. Cammerer, F. Ait Aoudia, M. Nimier-David, L. Maggi, G. Marcus, A. Vem, and A. Keller, "Sionna," 2022, <https://nvlabs.github.io/sionna/>.
- [45] P. Zheng, R. Wang, A. Shamim, and T. Y. Al-Naffouri, "Mutual coupling in RIS-aided communication: Model training and experimental validation," *IEEE Transactions on Wireless Communications*, vol. 23, no. 11, pp. 17 174–17 188, 2024.
- [46] Q. Spencer, A. Swindlehurst, and M. Haardt, "Zero-forcing methods for downlink spatial multiplexing in multiuser MIMO channels," *IEEE Transactions on Signal Processing*, vol. 52, no. 2, pp. 461–471, 2004.